

RESEARCH ARTICLE

10.1002/2016JC012483

Nonlinear multiscale interactions and internal dynamics underlying a typical eddy-shedding event at Luzon Strait

Yuan-Bing Zhao¹, X. San Liang^{1,2}, and Jianping Gan³

¹School of Atmospheric Sciences, Nanjing University of Information Science and Technology, Nanjing, China, ²School of Marine Sciences, Nanjing University of Information Science and Technology, Nanjing, China, ³Department of Mathematics, Hong Kong University of Science and Technology

Key Points:

- The observed warm eddy as Kuroshio passes Luzon Strait is not generated within the Kuroshio intrusion loop, but in Northwest Pacific
- The eddy is greatly strengthened as it propagates across the Kuroshio through a mixed instability
- An up-scale energy transfer west of the Dongsha Islands leads to the rapid demise of the eddy

Correspondence to:

X. S. Liang,
sanliang@courant.nyu.edu

Citation:

Zhao, Y.-B., X. S. Liang, and J. Gan (2016), Nonlinear multiscale interactions and internal dynamics underlying a typical eddy-shedding event at Luzon Strait, *J. Geophys. Res. Oceans*, 121, 8208–8229, doi:10.1002/2016JC012483.

Received 17 OCT 2016

Accepted 23 OCT 2016

Accepted article online 25 OCT 2016

Published online 11 NOV 2016

Abstract Eddy-shedding is a highly nonlinear process that presents a major challenge in geophysical fluid dynamics. Using the newly developed localized multiscale energy and vorticity analysis (MS-EVA), this study investigates an observed typical warm eddy-shedding event as the Kuroshio passes the Luzon Strait, in order to gain insight into the underlying internal dynamics. Through multiscale window transform (MWT), it is found that the loop-form Kuroshio intrusion into the South China Sea (SCS) is not a transient feature, but a quasi-equilibrium state of the system. A mesoscale reconstruction reveals that the eddy does not have its origin at the intrusion path, but comes from the Northwest Pacific. It propagates westward, preceded by a cyclonic (cold) eddy, through the Kuroshio into the SCS. As the eddy pair runs across the main current, the cold one weakens and the warm one intensifies through a mixed instability. In its development, another cold eddy is generated to its southeast, which also experiences a mixed instability. It develops rapidly and cuts the warm eddy off the stream. Both the warm and cold eddies then propagate westward in the form of a Rossby wave (first baroclinic mode). As the eddies approach the Dongsha Islands, they experience another baroclinic instability, accompanied by a sudden accumulation of eddy available potential energy. This part of potential energy is converted to eddy kinetic energy through buoyancy conversion, and is afterward transferred back to the large-scale field through inverse cascading, greatly reducing the intensity of the eddy and eventually leading to its demise.

1. Introduction

The Luzon Strait (LS), which is located between the Islands of Taiwan and Luzon, is the only deep-water channel connecting the South China Sea (SCS) and the Northwest Pacific (Figure 1). The LS has a width of approximately 350 km and a maximum depth of more than 2500 m, with Batan and Babuyan Islands lying in between. The ambient current system is complex. To its east is the subtropical countercurrent (STCC) area of strong baroclinic instability, where Rossby waves and eddy activities are extremely active [Qiu, 1999; Liu *et al.*, 2012]. Along the LS is Kuroshio, the famous western boundary current in the Northwest Pacific that transports warm and salty waters from the tropics to the midlatitudes, greatly impacting the Northern Hemisphere climate [e.g., Williams *et al.*, 2007]. As the Kuroshio passes by the LS, its path bends to the west due to the absence of a coast supporting the pressure gradient, exchanging mass, momentum, and energy with the SCS, and hence, affecting SCS circulation [Gan *et al.*, 2006]. Over the past few decades, extensive research has been conducted to examine Kuroshio intrusion into the SCS through the LS [see Hu *et al.*, 2000; Nan *et al.*, 2014].

Kuroshio intrusion is often followed by eddy shedding. Both observations [e.g., Yuan *et al.*, 2006; Caruso *et al.*, 2006] and numerical experiments [e.g., Farris and Wimbush, 1996; Chern and Wang, 1998; Sheremet, 2001; Xue *et al.*, 2004; Wu and Chiang, 2007; Chern *et al.*, 2010; Sheu *et al.*, 2010] have shown that, in winter, the Kuroshio in the LS frequently loops, which, when bent to a certain extent, can be easily cut off to shed warm anticyclonic vortices [Li *et al.*, 1998; Yuan *et al.*, 2006; Jia and Chassignet, 2011]. Nan *et al.* [2011b] examined the statistics of LS vortices and Kuroshio paths using 17 years of satellite observations. They found that the formation of the vortices is related to seasonal variation in the Kuroshio path and not the local wind stress. Theoretical studies [Sheremet, 2001] have also shown that the system may have multiple equilibria depending on its gap width and Reynolds number. As these parameters vary, the system may experience transitions from one state to another and exhibit hysteresis, leading to vortex shedding.

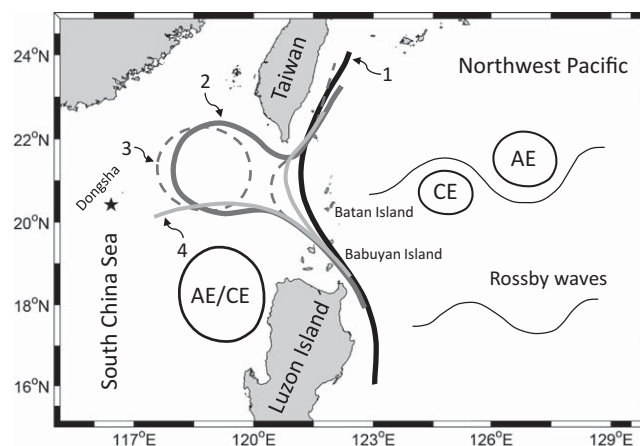


Figure 1. Schematic of currents and processes around the Luzon Strait. The thick black line (1) represents the “leaping path,” the dark gray curve (2) represents the “loop path,” the dashed line (3) represents the shed eddy, and the light gray line (4) represents the “leaking path.” Wavy curves indicate Rossby waves and circles represent eddies, with “AE” signifying anticyclonic eddies and “CE” signifying cyclonic eddies.

Conversely, the impingement of Rossby waves and westward vortices from the Northwest Pacific may also lead to eddy shedding. This has been studied with a 1.5-layer reduced gravity model [Yuan and Wang, 2011].

All these idealized models are instructive for illustrating certain impacts [Sheremet and Kuehl, 2007; Kuehl and Sheremet, 2009; Yuan and Wang, 2011]. However, they cannot demonstrate the combined effect of factors such as the real terrain [Metzger and Hurlburt, 2001], wind stress [Wang et al., 2010], bottom friction, and vertical stratification. How the Kuroshio intrudes and how the vortices shed in the real world remain important issues to be investigated.

Central to the eddy-shedding process is multiscale interaction, particularly mean-eddy interaction, which is a fundamental problem in geophysical fluid dynamics (GFD). However, due to the high nonlinearity and localness in both space and time, the problem has still not been resolved satisfactorily. Although many studies have been conducted on the interaction between the Kuroshio and eddies at the LS, they are mostly descriptive. Jia et al. [2005] carried out several numerical experiments with a 2.5-layer model to simulate the shedding and analyzed the energetic processes with a decomposition strategy based on the Reynolds method [McCreary and Yu, 1992]. They found that the energy for the shedding process comes primarily from the Kuroshio’s instability. However, their results are based on an idealized model whose reliability is yet to be validated. Moreover, the Reynolds method cannot effectively handle the highly intermittent process interactions, since the use of long-term averages implicitly assumes that the fields are stationary, which is contradictory to the fact that instabilities are essentially energy burst processes.

In this study, we focus on the diagnostics of multiscale energetics, which form convenient diagnostic quantities for the problem, as the instability of a background flow is essentially a process that transfers energy from the background flow to eddies. Classically, energetics are expressed in a bulk fashion, i.e., with spatial and temporal means applied. While this is certainly appropriate if one is satisfied with a global assessment of the system, in this problem, we are actually enquiring into the spatial and temporal structures of the instability, among others, in order to understand the burst process as identified above. In other words, we need to examine the localized multiscale energetics within the system. This turns out to be difficult, since in the classical framework, localization counteracts multiscale decomposition; the above Reynolds method is such an example. Continuing efforts have been invested in this field, which include the localized multiscale energy and vorticity analysis (MS-EVA) developed by Liang and Robinson [2005, 2007, hereinafter LR05 and LR07]. MS-EVA is a generic methodology for investigating the multiscale nonlinear interactive geophysical fluid flow processes that are, in nature, highly nonlinear and intermittent in space and time. It is rigorous in mathematics and physics, without invoking simplification or approximation, and has been applied successfully to different ocean, atmosphere, and engineering problems [e.g., Liang and Robinson, 2004, 2009]. Many problems that otherwise would be very difficult, if not impossible, to investigate turn out to be straightforward in this framework. Hence, we will apply MS-EVA to study a typical eddy-shedding event in the LS, and hopefully, give the questions, including the nonlinear interactions between the Kuroshio and eddy and the processes underlying the shedding, satisfactory answers.

The rest of the paper is organized as follows. In the next section, we describe the eddy-shedding event observed in late 1997 through early 1998. Section 3 describes how the data are prepared, and briefly introduces MS-EVA. The results and the analysis are presented in sections 4 and 5, respectively. Section 6 discusses the potential role of sub-mesoscale processes. This study is summarized in section 7.

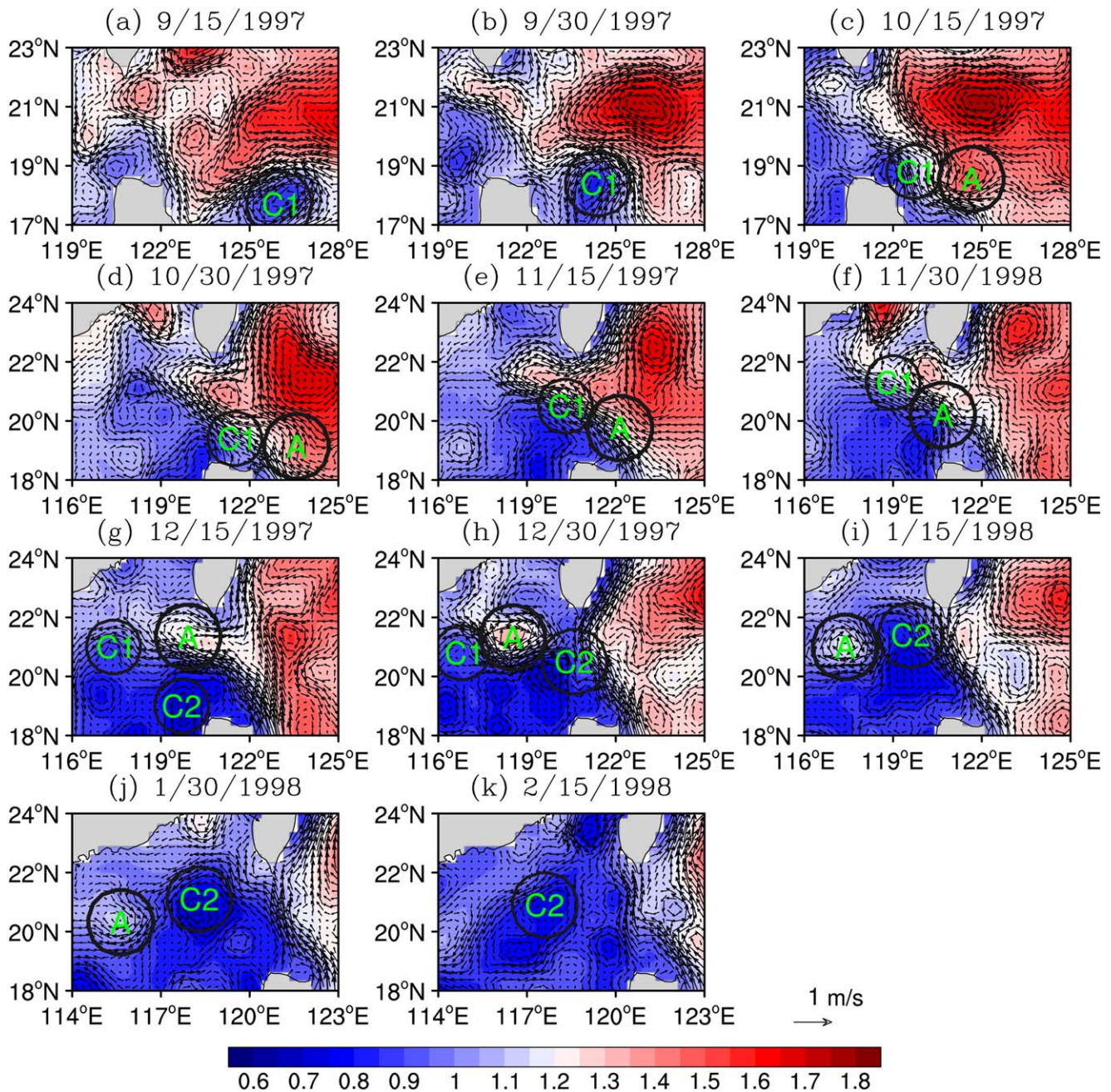


Figure 2. SSH (in m , shaded) and corresponding geostrophic current (in $m\ s^{-1}$, vector) derived from AVISO, with the circles marking the eddies in the mesoscale window. The cyclonic and anticyclonic eddies mentioned in the text are marked as C1, C2 and A, respectively. Note that, though some of them may not be discernible from the snapshots, they can be clearly seen in the mesoscale fields (cf. section 5.1.2).

2. A Typical Eddy-Shedding Event at the LS

The eddy-shedding event during late 1997 through early 1998, as shown in Figure 2, is revealed clearly in the latest version of the SSALTO/DUACS Absolute Dynamic Topography (ADT) product distributed by AVISO. This product is a daily gridded data set with a Cartesian $1/4^\circ \times 1/4^\circ$ resolution. It has been successfully applied to ocean studies over the SCS [e.g., Yuan *et al.*, 2006; Nan *et al.*, 2011a]. More information on the data can be obtained from the website (<http://www.aviso.altimetry.fr/en/data.html>). In September 1997, a strong cyclonic eddy (marked as C1 in the figure) to the east of Luzon moves westward (Figures 2a and 2b). By mid-October, it impinges onto the western boundary current and disappears (Figure 2c). Meanwhile, an

anticyclonic eddy (marked as A) appears to the east of where the cyclonic eddy vanishes. Later, this anticyclonic eddy crosses the Kuroshio and disappears, too (Figure 2d). In the meantime, the Kuroshio starts to intrude into the SCS in the form of a loop. During almost the same period, a cyclonic vortex forms to the northwest of the Luzon Island, referred to as the Luzon Cold Eddy [e.g., Shaw *et al.*, 1999; Qu, 2000] or Luzon Cyclonic Gyre (LCG) [e.g., Nan *et al.*, 2011a] in previous studies. Hereafter, we prefer the latter in order to distinguish it from the mesoscale eddies discussed in the following sections. With time, the LCG develops while moving to the north, forming a barrier to Kuroshio intrusion (Figure 2e). Meanwhile, an anticyclonic gyre (not shown) develops to the east of Luzon, strengthening the horizontal pressure gradient across the Kuroshio (Figure 2f). By mid-December, the Kuroshio flows into the SCS to the northeast of Luzon Island with a small incident angle, and after passing through the Batan Islands, it follows a sharp curved path, and then travels westward along the LCG's northern edge (Figure 2g). At this time, the loop center is situated more westward and is zonally stretched. Later on, the center moves further westward and tends to depart from the main current, whereas the LCG extends northward and cuts off the connection between the loop and the main current (Figure 2h) and forms a cold eddy (denoted as C2). The detached eddy (marked as A in the figure) has a diameter of 200 km, which agrees with previous reports [e.g., Li *et al.*, 1998]. After departing from the Kuroshio, the eddy moves to the southwest along the steep continental shelf (Figure 2i), and eventually vanishes, after passing through the Dongsha Islands (Figures 2j and 2k).

Note that, though the shedding can be clearly seen from the observations, some of the eddy paths may be not easy to discern in the original fields alone. This will be clearer later in section 5.1.2 in the decomposed mesoscale fields.

3. Data Set and Method

3.1. Data Set

We use the Regional Ocean Model System (ROMS) [Shchepetkin and McWilliams, 2005] to simulate the observed shedding and then conduct the MS-EVA analysis. The model domain is chosen to be 15°N – 27°N, 114°E – 128°E (cf. Figure 1). The grid has a horizontal resolution of 1°/16 (~ 6.5 km), with 32 levels in the vertical direction, and 223×206×32 points in total. The minimum and maximum water depths are set to be 15 m and 6000 m, respectively.

The model is initialized with the HYCOM reanalysis data (<http://hycom.org/dataserver/glb-reanalysis>) of 1 August 1997 [Fox *et al.*, 2002; Cummings, 2005]. This data set has been systematically evaluated [Kara *et al.*, 2008] and used to investigate the ocean processes in the LS [e.g., Lu and Liu, 2013]. At the surface, the model is driven by atmospheric forcing and horizontal boundary fluxes, which are derived from CFSR NCAR. The velocity and tracer fields used for the lateral boundary conditions [Marchesiello *et al.*, 2001] are interpolated from the daily HYCOM 1°/12 global reanalysis (as used in the initial condition), whereas the SSH is derived from AVISO's absolute dynamic topography. In this study, tides are excluded. Besides, following Yang *et al.* [2011], the model SSH is nudged to AVISO ADT within the whole domain. We tried several nudging time scales (τ_{out}) and found $\tau_{out}=1$ day to be the best. The model starts from 1 August 1997, and ends on 1 May 1998. The time steps (Δt) for the baroclinic and barotropic modes are 300 s and 5s, respectively. The outputs, including surface elevation, u , v , w , ρ , and tracers, are saved every 12 h.

The simulation output is carefully evaluated. Although the HYCOM data and AVISO observations are incorporated into the ROMS in the hope of achieving a better simulation, not much is gained here. Nevertheless, the model results reveal an eddy-shedding event very similar to that observed by AVISO. Specifically, the model SSH and surface velocity fields appear almost the same as those in Figure 2, only with a time delay. This delay may result from the boundary conditions extracted from HYCOM, which lags AVISO ADT during this period. However, the key features (eddies) described in section 2 are well reproduced. We therefore use the model output for this study.

3.2. Localized Multiscale Energy and Vorticity Analysis (MS-EVA)

The research methodology for this study is the multiscale energetics part of the localized multiscale energy and vorticity analysis, or MS-EVA for short (cf. LR05); also to be used is the MS-EVA-based theory of localized finite-amplitude baroclinic and barotropic instabilities (LR07). This is a systematic line of work, involving ingredients from different disciplines such as functional analysis and geophysical fluid dynamics. A detailed

introduction of MS-EVA is beyond the scope of this study; in this section, we present a very brief introduction. For details and comparison with traditional local and global energetics formalisms, refer to the previous publications (e.g., LR05 and LR07) and the references therein.

MS-EVA is based on a new functional analysis tool, called multiscale window transform (MWT) [Liang and Anderson, 2007]. Using MWT, one can split a function space into a direct sum of several mutually orthogonal subspaces, each with an exclusive range of time scales, while preserving its time locality properties. Such a subspace is termed a *scale window* or simply a *window*. One may have as many windows as they wish; for this study, we need three, namely a large-scale window (mean window), a mesoscale window (eddy window), and a sub-mesoscale window (turbulence window). For easy reference, they are denoted as $\varpi=0, 1, \text{ and } 2$, respectively. These windows can be demarcated on the wavelet spectrum by three “window bounds”: $j_0, j_1, \text{ and } j_2$, which are the upper wavelet scale levels. In other words, given a series scaled with time span $\tau, \tau \cdot 2^{-j_0}, \tau \cdot 2^{-j_1}, \text{ and } \tau \cdot 2^{-j_2}$ are upper-scale bounds, respectively, for these three windows.

For a given series $S(t)$, MWT application yields two types of quantities: one is the MWT coefficients, \widehat{S}_n^{ϖ} , and the other is the multiscale window reconstruction (MWR), $S^{\sim\varpi}(t)$, for $\varpi=0, 1, \text{ and } 2$. MWT and MWR form a transform pair, but are different concepts – with the former defined in phase space and the latter defined in physical space. For example, the MWR of $S(t)$ on the mesoscale window corresponds to a band-pass-filtered signal, whereas the MWT of $S(t)$ is different. MWT has many nice properties, one being the *Property of Marginalization*, which allows for a precise representation of multiscale energy (actually applicable to any quadratic quantity) as the product of the MWT coefficients (up to some constant). For example, the eddy energy extracted from $S(t)$ is simply $(\widehat{S}_n^{\sim 1})^2$ multiplied by some constant. (In a two-window decomposition, since $S(t)=S^{\sim 0}(t)+S^{\sim 1}(t)$, the eddy energy is usually expressed as $(S^{\sim 1})^2$. This is, however, conceptually wrong. One immediately finds its inadequacy by observing that $(S^{\sim 0})^2+(S^{\sim 1})^2 \neq S^2$. In fact, multiscale energy is a concept in phase space (expressed with transform coefficients, such as $\widehat{S}_n^{\sim 1}$), which connects to physical energy through the Parseval relation in functional analysis, analogous to a Fourier spectrum. Attempting to represent it using reconstructed fields (such as the above $S^{\sim 1}$) is useless. In fact, this is the very difficulty with classical filters, which only produce the above reconstructed fields, and hence, cannot represent energy; this problem has not been well formulated until wavelets and filter banks are connected [Strang and Nguyen, 1996].) Since $\widehat{S}_n^{\sim 1}$ is localized, where the location is labeled as n in the time domain, this essentially solves the oddity between localization and multiscale decomposition.

One may argue that orthonormal wavelet transforms (the concept of energy can only be introduced with orthogonal transforms) are just for tackling such problems. In this case, we are studying eddies, which are defined on a range of scales, or scale windows as introduced above, rather than individual scales. To represent the energy of an eddy, we must summarize the energies over the scale levels within the window. However, for an orthonormal wavelet transform, the transform coefficients for different scale levels are discretely defined at different locations, making the summation impossible. In contrast, MWT is a transform with respect to individual scale windows, rather than individual scales, and hence, does not have this difficulty.

It should be mentioned that, just as with wavelet analysis, a compromise between localization in time and frequency is inherent in MWT as well. Therefore, in practice, localization is smeared out.

MWT application to primitive equations yields localized multiscale energetics. However, one issue remains, that is, distinguishing transfer and transport processes from the intertwined nonlinear terms. For a scalar field S within a flow \mathbf{v} , the energy transfer from other scale windows to window ϖ rigorously proves (LR05) to be

$$T_n^{\varpi} = -E_n^{\varpi} \nabla \cdot \mathbf{v}_S^{\varpi}, \tag{1}$$

where $E_n^{\varpi} = \frac{1}{2} (\widehat{S}_n^{\sim\varpi})^2$ is the energy on window ϖ at step n (e.g., if S is density anomaly, then E_n^{ϖ} is APE; refer to LR05 for a detailed explanation), and

$$\mathbf{v}_S^{\varpi} = \frac{(\widehat{\mathbf{v}S})_n^{\sim\varpi}}{\widehat{\mathbf{v}}_n^{\sim\varpi}} \tag{2}$$

is referred to as the *S-coupled velocity*. This transfer possesses a very interesting property, namely

Table 1. Symbols for Multiscale Energetics (Time Step n , Scale Window ϖ)^a

Kinetic Energy (KE)		Available Potential Energy (APE)	
\dot{K}_n^ϖ	Time rate of change of KE	\dot{A}_n^ϖ	Time rate of change of APE
$T_{K_n}^\varpi$	Total KE transfer	$T_{A_n}^\varpi$	Total APE transfer
$\Delta Q_{K_n}^\varpi$	KE advective working rate	b_n^ϖ	Rate of buoyancy conversion
$\Delta Q_{P_n}^\varpi$	Pressure working rate	$\Delta Q_{A_n}^\varpi$	APE advective working rate

^aFor details, refer to Liang and Robinson [2005].

$$\sum_{\varpi} \sum_n T_n^\varpi = 0, \tag{3}$$

as proved in LR05. Physically, this implies that the transfer is a mere redistribution of energy among the scale windows, without generating or destroying energy as a whole. This property, though simple to state, does not hold in previous energetic formalisms (refer to LR07 for a clear comparison to the classical formalism; in particular, compare the traditional two-scale energy equations, (2) and (3), to the equations resulting from MS-EVA, (19) and (20)). To distinguish it from those that may have been encountered in the literature, the above transfer is termed *canonical transfer*. Historically, it has been referred to as the “perfect transfer.”

With MWT, the kinetic energy (KE) and available potential energy (APE) densities (for convenience, we will simply refer to them as KE and APE, unless confusion may arise) for window ϖ at time step n can be defined, following Lorenz [1955], as

$$K_n^\varpi = \frac{1}{2} \rho_0 \widehat{\mathbf{v}}_{H,n}^\varpi \cdot \widehat{\mathbf{v}}_{H,n}^\varpi, \tag{4}$$

$$A_n^\varpi = \frac{1}{2} c (\widehat{\rho}_n^\varpi)^2. \tag{5}$$

In the above definitions, ρ_0 is the reference density (here taken as 1025 kg m^{-3}); \mathbf{v}_H is the horizontal velocity; ρ is the density anomaly (with the mean vertical profile $\bar{\rho}(z)$ removed); and $c = g^2 / (\rho_0 N^2)$, where N is the buoyancy or Brunt-Väisälä frequency. The evolution equations of K_n^ϖ and A_n^ϖ in the absence of diffusion/dissipation can now be obtained as follows (LR05):

$$\begin{aligned} \frac{\partial K_n^\varpi}{\partial t} + \underbrace{\nabla \cdot \left[\frac{1}{2} \rho_0 \widehat{\mathbf{v}}_n^\varpi (\widehat{\mathbf{v}}_H)_n^\varpi \right]}_{\Delta Q_{K_n}^\varpi} + \underbrace{\nabla \cdot (\widehat{\mathbf{v}}_n^\varpi \widehat{\rho}_n^\varpi)}_{\Delta Q_{P_n}^\varpi} = \\ - \underbrace{\frac{1}{2} \rho_0 [(\widehat{u}_n^\varpi)^2 \nabla \cdot \widehat{\mathbf{v}}_u^\varpi + (\widehat{v}_n^\varpi)^2 \nabla \cdot \widehat{\mathbf{v}}_v^\varpi + (\widehat{w}_n^\varpi)^2 \nabla \cdot \widehat{\mathbf{v}}_w^\varpi]}_{T_{K_n}^\varpi} - \underbrace{g \widehat{\rho}_n^\varpi \widehat{w}_n^\varpi}_{b_n^\varpi}, \end{aligned} \tag{6}$$

$$\frac{\partial A_n^\varpi}{\partial t} + \underbrace{\nabla \cdot \left[\frac{1}{2} c \widehat{\rho}_n^\varpi (\widehat{\rho}_n^\varpi) \right]}_{\Delta Q_{A_n}^\varpi} = \underbrace{-A_n^\varpi \nabla \cdot \widehat{\mathbf{v}}_\rho^\varpi}_{T_{A_n}^\varpi} + \underbrace{g \widehat{\rho}_n^\varpi \widehat{w}_n^\varpi}_{b_n^\varpi} + \underbrace{\frac{1}{2} \widehat{\rho}_n^\varpi (\widehat{\rho}_w)_n^\varpi \frac{\partial c}{\partial z}}_{TS_{A_n}^\varpi}, \tag{7}$$

for $\varpi=0, 1$, and 2 , where $\widehat{\mathbf{v}}_S^\varpi$ is the coupled velocity for $S=u, v, w, \rho$, and others (g and ρ) are conventional. In equations (6) and (7), the ΔQ terms stand for energy flux divergences ($\Delta Q_{K_n}^\varpi, \Delta Q_{A_n}^\varpi$) or pressure work ($\Delta Q_{P_n}^\varpi$) on the designated scale window. For analysis, they are further divided into two components: the horizontal component ($\Delta_h Q$) and the vertical component ($\Delta_z Q$). The b terms are the rates of buoyancy conversion between APE and KE on the designated scale windows, and the T terms are the canonical transfers among different windows. An extra term ($TS_{A_n}^\varpi$) exists on the *r.h.s* of equation (7) due to the vertical shear of c . This is an apparent source/sink arising from the APE definition, which is usually negligible. Other notations are summarized in Table 1. Note that all terms are localized in both space and time; in other words, they are all four-dimensional field variables, quite different from the classical formalisms in which localization is lost at least in one dimension of space-time to achieve the scale decomposition. Processes intermittent in space and time are thus naturally embedded in equations (6) and (7). A schematic of the flowchart is shown in Figure 3.

It has been established that the canonical transfer terms ($T_{K_n}^\varpi$ and $T_{A_n}^\varpi$) in equations (6) and (7) correspond precisely to the two important geophysical fluid flow processes, i.e., barotropic instability and baroclinic

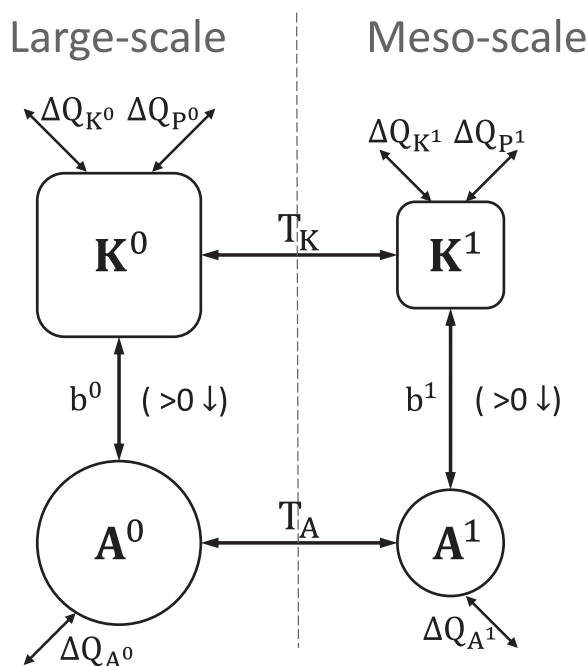


Figure 3. Schematic of MS-EVA energetics for a two-scale window decomposition. Symbols are conventional in MS-EVA studies (refer to Table 1), with superscripts 0 and 1 signifying large-scale window and mesoscale window (or “eddy” window), respectively. Buoyancy conversion is defined to be positive if it is from KE to APE. This schematic is a simplified version of the three-window energy flowchart shown in Liang and Robinson [2005, Figure 7].

variables are interpolated onto 13 flat z-levels, which are summarized in Table 2. The series used for the analysis spans from 18 August 1997, to 1 May 1998, with a time interval $\Delta t = 12$ h and 2^9 time steps in total, which is sufficiently long to cover the complete life cycle of the observed anticyclonical shed eddy. For APE analysis, a mean profile of $\bar{\rho} = \bar{\rho}(z)$ is necessary, and is obtained by averaging ρ over all available data points and time instants.

The scale window bounds are usually determined through spectral analysis. However, the determination can be simplified here. According to the description above, the life cycle of the detached eddy from the Kuroshio lasts about 2 months, from the beginning of December 1997 to the beginning of February 1998. This observation yields a rough approximation in the large-scale and mesoscale bounds, $j_0 = 2$ and $j_1 = 5$, respectively (corresponding to 128 and 16 days). Namely, the low-frequency variabilities (>128 days) are placed in the large-scale window; those located between 16 and 128 days are placed in the mesoscale window, and the others are placed in the sub-mesoscale window. We have also tested other scale window demarcations, e.g., $(j_0, j_1) = (2, 6)$, and the results are almost the same. Table 2 summarizes the parameters necessary for analysis.

5. Analysis Results

With the data sets generated and the parameters set in Table 2, a three-scale decomposition is performed for each field. Since the aim of this study is to investigate the eddy-shedding process, namely the interaction

Table 2. Parameters for the MS-EVA Application	
Parameters	Value
Time window bounds: j_0, j_1	2, 5 (128 days, 16 days)
Grid	$195 \times 174 \times 13 \times 512$
Time stepsize Δt	12 h
Horizontal grid spacing $\Delta x, \Delta y$	6471 m
Vertical level depths (13 levels, in meters)	1, 3, 5, 8, 20, 45, 80, 125, 175, 250, 350, 450, 575

instability (LR07); details are present in a recent comprehensive review paper [Liang, 2016]. For notational convenience, they are written as BT and BC, respectively. A criterion is then derived in LR07 for instability identification:

1. A flow is locally unstable if $BC + BT > 0$, and vice versa
2. For an unstable system, if $BT > 0$ and $BC \leq 0$, the instability is barotropic
3. For an unstable system, if $BC > 0$ and $BT \leq 0$, then the instability is baroclinic
4. If both BT and BC are positive, the system is undergoing a mixed instability.

Because of their physical meanings, in the following sections, we may refer to BT and BC as barotropic transfer and baroclinic transfer, respectively.

4. MS-EVA Setup

The fields required in MS-EVA include velocity (u, v , and w), density (ρ), and pressure (p). In the vertical direction,

between the mesoscale eddy and the Kuroshio, the analysis is performed with respect to the large-scale and mesoscale windows.

Strictly speaking, we are actually talking about “slowly- and fast-evolving fields” or “long- and intermediate-time scales” since the decomposition in this study is

performed only in the time dimension. However, there is a close relationship between time scale and spatial scale in ocean processes, which is the case in this problem. We hence do not distinguish these terms here.

5.1. Reconstructed Fields on Multiscale Windows

5.1.1. Large-Scale Fields

Figure 4 shows the reconstructed large-scale velocity and temperature fields at 250 m. From mid-September to early December, the warm Kuroshio flows northwestward into the SCS (Figure 4a). When it reaches the east of the Dongsha Islands, the flow splits into two branches. The main branch rotates anticyclonically and flows eastward out of the SCS along the south coast of Taiwan, forming a loop structure, and the other branch flows toward the Dongsha Islands along the continental shelf. Another slowly varying feature is the LCG to the west of Luzon Island. The LCG first appears at the end of October 1997, developing with time (Figures 4a and 4b), with a horizontal scale of up to 400 km. Meanwhile, the loop branch of the Kuroshio weakens substantially, and more Kuroshio water intrudes into the SCS in the form of a leaking path [e.g., Nan et al., 2014], which flows to the west along the northern edge of the LCG. By the end of December 1997 (Figure 4c), the LCG is fully developed and the loop path of the Kuroshio is degenerated into a leaping path. By 30 January 1998, the LCG tends to disappear (Figure 4d). As a result, the branch of the intruded Kuroshio is pushed to the north and flows southwestward along the continental shelf.

In this study, the large-scale window is above 128 days. Thus, the slowly varying feature further implies that the loop path, which remains for 3 months from September to late December, is one of the quasi-equilibrium solutions of the Kuroshio state and not a transient phenomenon [e.g., Sheremet, 2001; Yuan et al., 2006].

5.1.2. Mesoscale Fields and the Origins of the Three Eddies

The reconstructed mesoscale fields reveal eddy-like features, most of which are barely observable from the original maps (Figure 2). To record the life cycle of the shedding, we sample the time sequence every 15 days from 15 October, and draw the plots in Figure 5. As above, we only analyze the 250 m level.

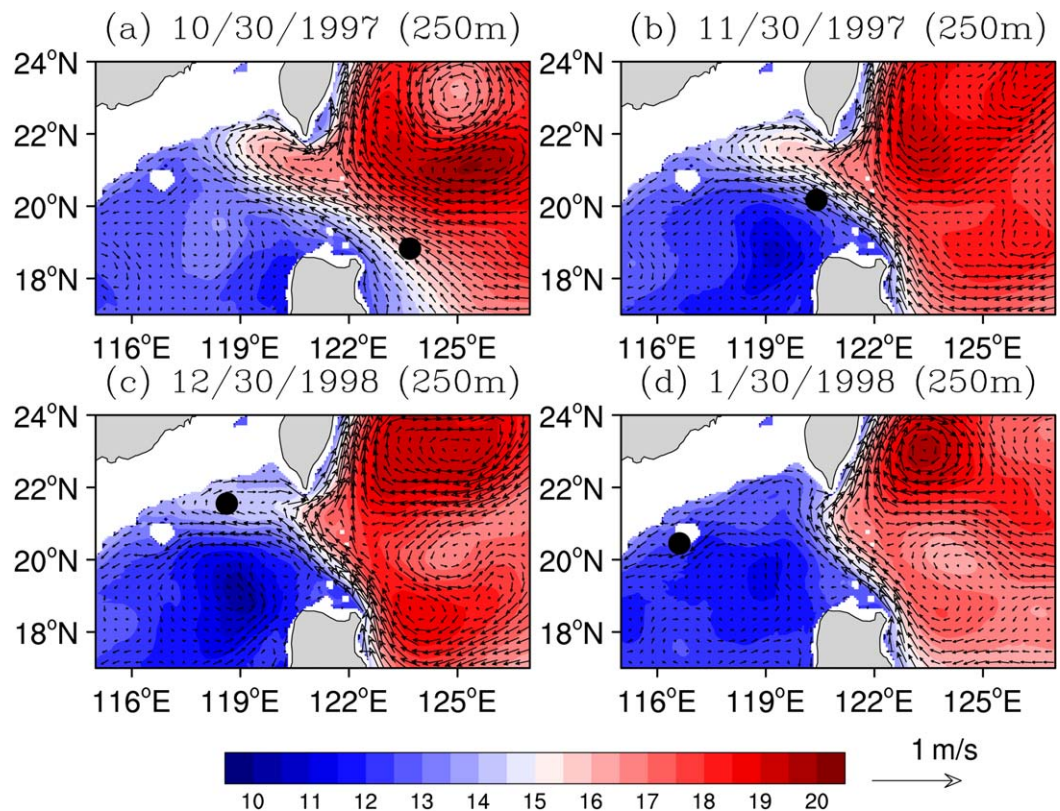


Figure 4. Reconstructed large-scale velocity (in $m s^{-1}$, vector) and temperature (in $^{\circ}C$, shaded) at 250 m, with the black dot indicating the location of eddy A.

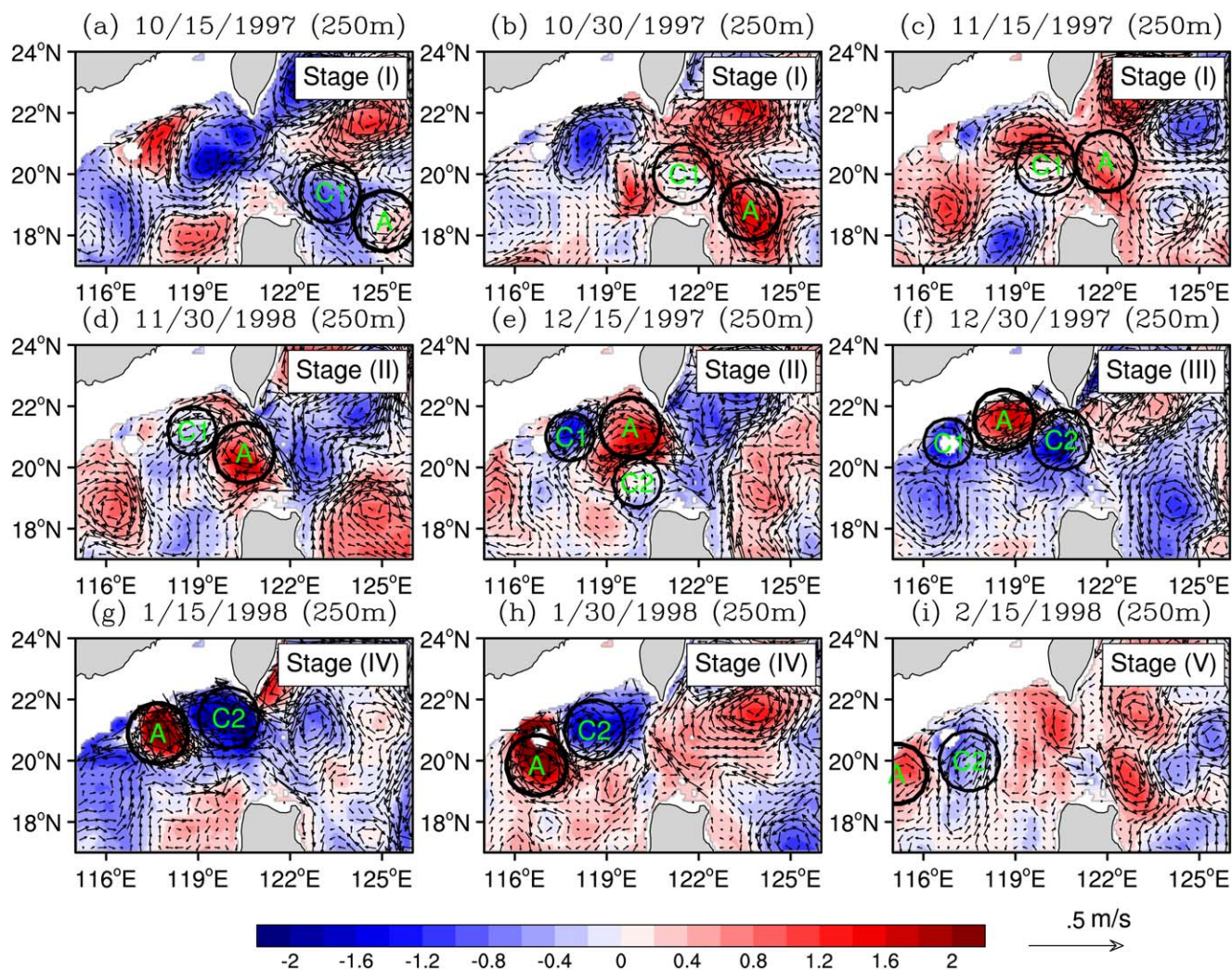


Figure 5. Same as Figure 4, but for mesoscale fields, with the circles marking eddies and legends denoting different stages, as discussed in the text.

Generally, the maps in Figure 5 are characterized by cyclonic eddies accompanied by cold centers and anticyclonic eddies accompanied by warm centers. For convenience, three eddies, which are related to this shedding process, are marked by black circles. The warm anticyclonic one is labeled “A,” and the two cold cyclonic ones are indicated by “C1” and “C2.” As shown in section 2, the eddy-shedding event is preceded by an interaction between the Kuroshio and a strong cyclonic eddy from the western Pacific, and one may have an impression that the detached anticyclonic eddy originates within the loop area of the Kuroshio. Surprisingly, it is found from the reconstructed mesoscale fields that both the cyclonic and anticyclonic eddies have their origins in the Northwest Pacific.

In early October, eddy C1 approaches Luzon Island from the open ocean, followed by eddy A (Figure 5a). As C1 crosses the Kuroshio, it deforms, stretching along the high-speed western boundary current, and decays, but does not completely dissipate (Figures 5a and 5b). After entering the main current, both eddy C1 and eddy A grow, with the latter growing more conspicuously. By the end of November (Figure 5d), eddy A has reached the middle of the LS, with a horizontal scale of 200 – 300 km and a vertical extent of over 500 m (not shown). From early to mid-December, eddy A travels northwestward into the loop, whereas eddy C1 travels southwestward along the continental shelf (Figure 5e). Meanwhile, another cyclonic vortex (C2) appears south of eddy A, which develops and moves to the north, cutting the warm eddy off from the main current (Figure 5f). By mid-January 1998, eddy C1 has passed Dongsha and disappeared west of the islands (Figure 5g). Later (late January to mid-February), eddy A and eddy C2 also pass Dongsha and rapidly decay

there (Figures 5h and 5i). The above features and processes, some of which seem to be counterintuitive, are not easily observed in the original fields (Figure 2); only the cold eddy C1 is clearly observed in the original flow fields.

The eddy propagation speeds can be estimated from the locations of the eddy centroids, which are defined as the positions of minimum speed (sometimes as the center of extreme temperature if minimum speed is ambiguous) at 250 m. From the middle to the end of November, the warm eddy A crosses the Kuroshio, with significant change in velocity (velocity of the centroid; from 0.35 m s^{-1} to 0.15 m s^{-1}). During its mature period, it has a centroid speed of 0.15 m s^{-1} and a diameter of 250 km (two times the distance between the eddy centroid and maximum speed point), agreeing with the characteristics of the Rossby waves at 20°N revealed by both theoretical and observational results [e.g., Chelton *et al.*, 2007; Lin *et al.*, 2014].

5.2. Multiscale Energy

5.2.1. Large-Scale Available Potential Energy (MAPE) and Kinetic Energy (MKE)

Figure 6 shows the horizontal MAPE distribution at 175 m and the vertical structure along 19°N . Three maximum centers can be identified, which correspond well to the large-scale gyres in Figure 4. Particularly, the one to the west of Luzon corresponds to the LCG and the east one to the anticyclonic gyre. Moreover, MAPE in the LCG area begins accumulating in November (Figure 6a) and reaches a maximum in the mid-December (Figure 6b). As discussed in previous studies, the LCG is mostly wind driven [Qu, 2000]. Therefore, the large amount of MAPE may result from the wind through buoyancy conversion. When the Ekman transport in the upper boundary layer is inhomogeneous, its divergence can result in vertical motion (w'), which is always accompanied by a density anomaly (ρ') because of the stratification. This process is called buoyancy conversion ($\sim \rho' w'$), which is related to the APE generation [e.g., Gill *et al.*, 1974]. In the vertical direction, MAPE is largely concentrated between 50 and 400 m, with a maximum around 200 m (Figures 6e–6h).

Compared to MAPE, the large-scale kinetic energy (or mean KE, MKE) is more localized in space. The two areas with a large MKE are observed sitting northeast of Luzon and east of Taiwan, respectively (Figures 7a–7d). Their time evolutions reflect the variation in the path and strength of the Kuroshio current. As opposed to MAPE, MKE dominates primarily above 200 m. It is surface-trapped and decreases with depth (Figures 7e–7h).

5.2.2. Mesoscale Available Potential Energy (EAPE) and Kinetic Energy (EKE)

Figures 8 and 9 show the vertically integrated EAPE and EKE, respectively. Their distributions are quite contrasted, and these patterns are independent of the eddy's polarity; i.e., they hold for both cyclonic and

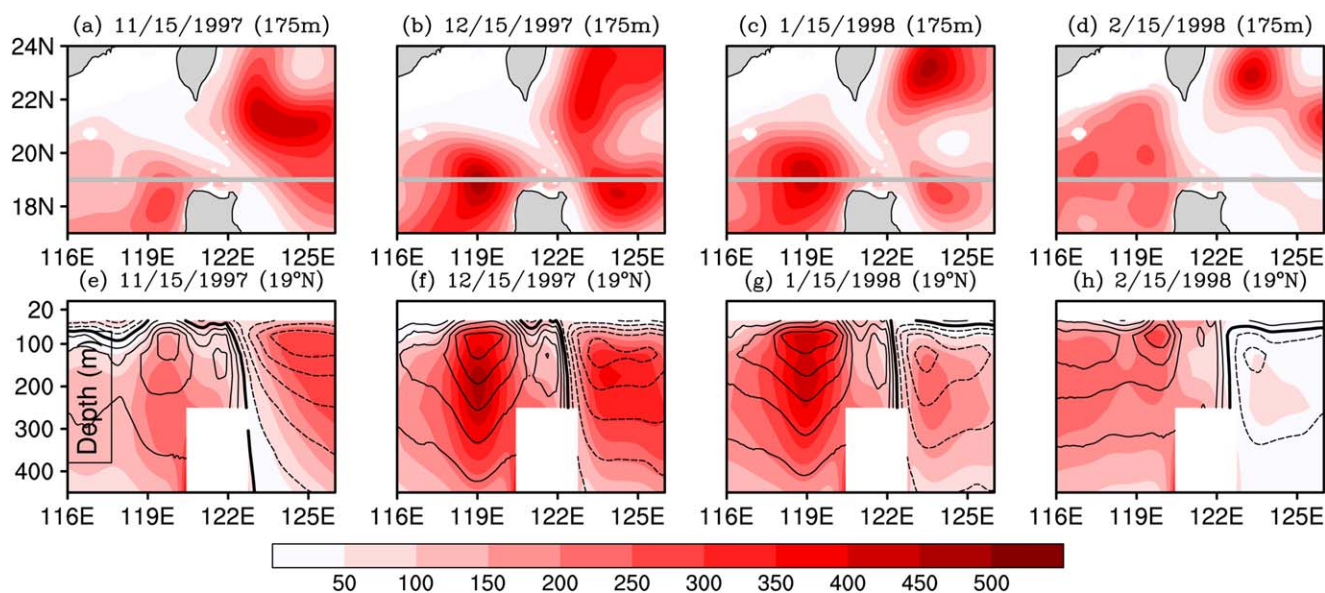


Figure 6. (a–d) MAPE at 175 m (in J m^{-3}) and (e–h) vertical section along 19°N . The line in Figures 6a–6d shows the position where the vertical section is taken. Contours in Figures 6e–6h stand for large-scale density anomaly (in kg m^{-3}), with solid lines for positive and dashed ones for negative.

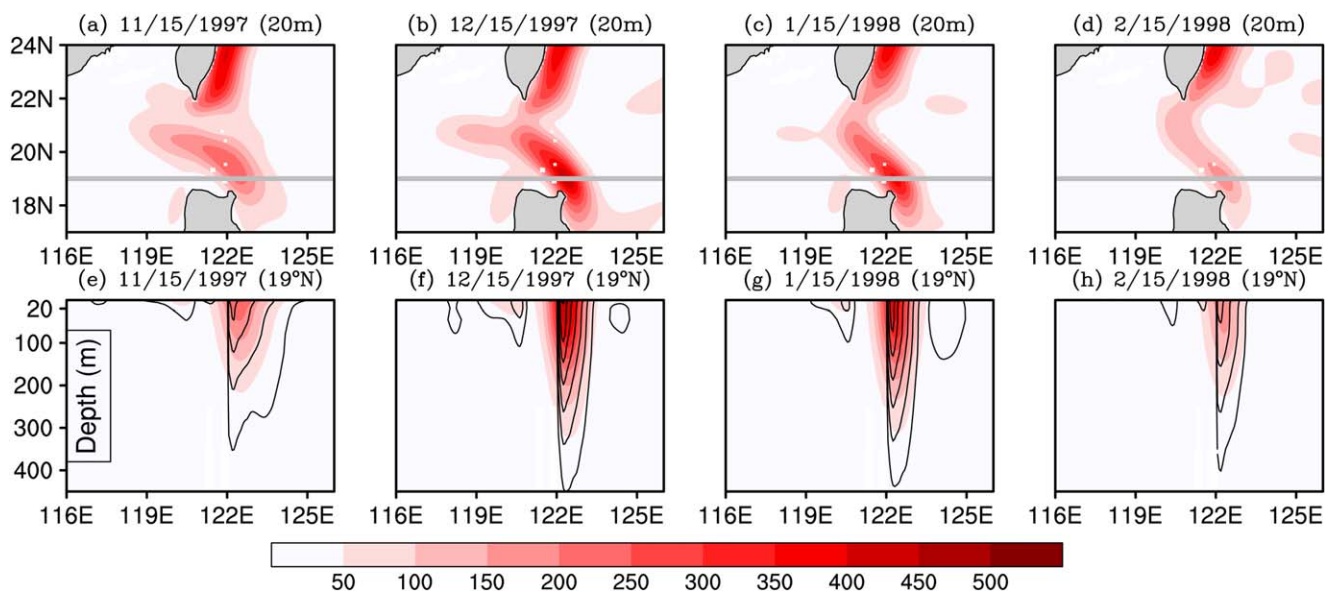


Figure 7. (a–d) Same as Figure 6, but for MKE at 20 m. (e–h) Contours are for the magnitude of horizontal speed (in m s^{-1}).

anticyclonic eddies. This phenomenon is consistent with the Gulf Stream ring observation by Barrett [1971], but different from that identified by Chu *et al.* [2014], which concludes that the vertically integrated EKE and EAPE have similar horizontal distributions.

In terms of time evolution, EAPE and EKE are in pace with each other. Recall that the purpose of this study is to analyze the anticyclonic eddy A (Figures 8 and 9), i.e., the eddy “detached from the Kuroshio.” For convenience, we divide the time sequence of its evolution into five stages: Stage I (15 October to 15 November; eddy crossing the Kuroshio), Stage II (15 November to 15 December; enhancement after crossing the Kuroshio), Stage III (15–30 December; eddy staying within the loop), Stage IV (30 December to 30 January; second enhancement), and Stage V (after 30 January; decaying). During the first stage, the eddy approaches the Kuroshio from the east. Both EAPE and EKE grow (Figures 8a, 8b, 9a, and 9b) and then decrease (Figures 8c and 9c). After crossing the Kuroshio, the eddy develops and accumulates EAPE and EKE rapidly (Figures 8d and 9d). Later, it moves to the loop area and remains there (15–30 December; Figures 8e, 8f, 9e, and 9f). Following the shedding event (25 December), the eddy moves again, directly toward Dongsha. During this period, both EAPE and EKE experience another enhancement (Figures 8g and 9g). As the eddy passes the islands, EAPE and EKE decay rapidly (Figures 8h, 8i, 9h, and 9i), and finally, it disappears.

We are interested in how much energy the eddy carries and how the ratio of EAPE to EKE varies with time. We then compute the eddy-volume-integrated EAPE and EKE. The computation is fulfilled in an eddy-following frame as follows: 1) choose the eddy center as the origin and draw a circle with a radius of 125 km (by the observation earlier on, the eddy has an average diameter of 250 km); 2) integrate the EAPE and EKE densities over the disk and *w.r.t.* z down to the bottom of the eddy. We also test two other radii, 100 km and 150 km, and the results are similar, as shown in Figure 10a. From the figure, one can identify three peaks, which correspond to Stage I, Stage II, and Stage IV, respectively. Generally, EAPE and EKE correlate well, but a closer observation reveals that the variation in EAPE falls somewhat behind that in EKE. Quantitatively, they can be as low as 1.5×10^{14} J and as high as 1.25×10^{15} J. Over its entire life cycle, the ratio EKE/EAPE may fluctuate between 0.4 and 1.6. However, during the mature period (Stages III and IV), the mean EAPE is 6.39×10^{14} J and the mean EKE is 7.20×10^{14} J, yielding an EKE/EAPE ratio of 1.13, i.e., a roughly equal partition between EKE and EAPE. This value is comparable to those of previous studies [e.g., Gill *et al.*, 1974; Reid *et al.*, 1981]. In the quasi-geostrophic framework, given the wavenumber k and the Rossby deformation radius of the first baroclinic mode $L_d = NH/f$, where $N = \sqrt{-g\bar{\rho}_z/\rho_0}$ is the buoyancy frequency, H is the water depth, and f is the Coriolis parameter, EKE/EAPE is of the order $(L_d/L)^2$, where L ($\sim 1/k$) is the length scale of the motion. For this problem, $k = 1.26 \times 10^{-5} \text{ m}^{-1}$, $g = 9.8 \text{ m s}^{-2}$, $f_{20^\circ\text{N}} = 4.99 \times 10^{-5} \text{ s}^{-1}$, $H = 500 \text{ m}$, $\rho_0 = 1025 \text{ kg m}^{-3}$, $\bar{\rho}_z = -7.3 \times 10^{-4} \text{ kg m}^{-3}$, and we obtain EKE/EAPE = 1.11.

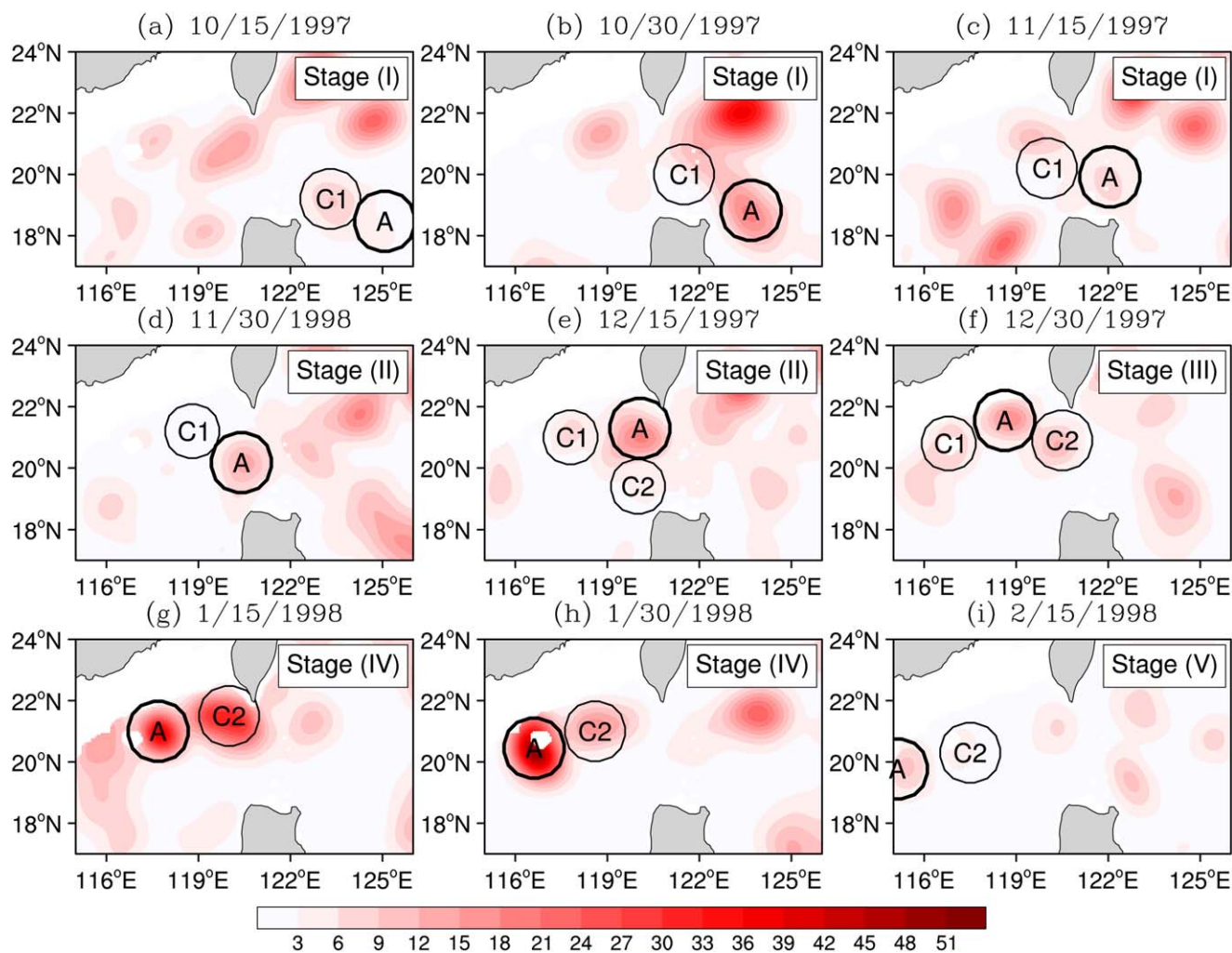


Figure 8. Vertically integrated EAPE (in 10^3 J m^{-2}). Eddies are marked in black circles and stages are denoted in boxes.

To reveal the vertical structure of EAPE and EKE for the eddy, we integrate the energy density over the horizontal disk at each level. Figure 10b shows the result for the mature period (Stages III and IV). Similar to the MAPE in Figure 6, EAPE concentrates between 50 and 400 m, and is maximized at 100 m. In contrast, EKE is surface trapped and dominates above 300 m. These structures are in agreement with previous results by, e.g., Barrett [1971], Gill *et al.* [1974], Reid *et al.* [1981], and Chu *et al.* [2014].

5.3. Energy Transfer and Energy Conversion

From above, we know that the eddy energy changes dramatically in nearly every stage except in Stage III. This section describes how EAPE and EKE are supplied or consumed.

5.3.1. Baroclinic Transfer (BC)

As reviewed in section 3.2, the baroclinic transfer (BC) measures the strength of baroclinic instability. Figure 11 shows a sequence of BC for the study domain. In mid-October, it is negative in the LS (Figure 11a). Starting from the end of October, a positive center begins to emerge in the LS and lasts through the beginning of February 1998 (Figures 11c–11h). In the east of the strait, BC first takes positive and negative values, respectively, south and north of 18°N (Figures 11a and 11b). Subsequently, starting from November, the pattern reverses and remains the same through February of the following year (Figures 11d–11i). In the vertical direction, the interaction process takes place mainly above 400 m, with its maximum around 200 m (not shown).

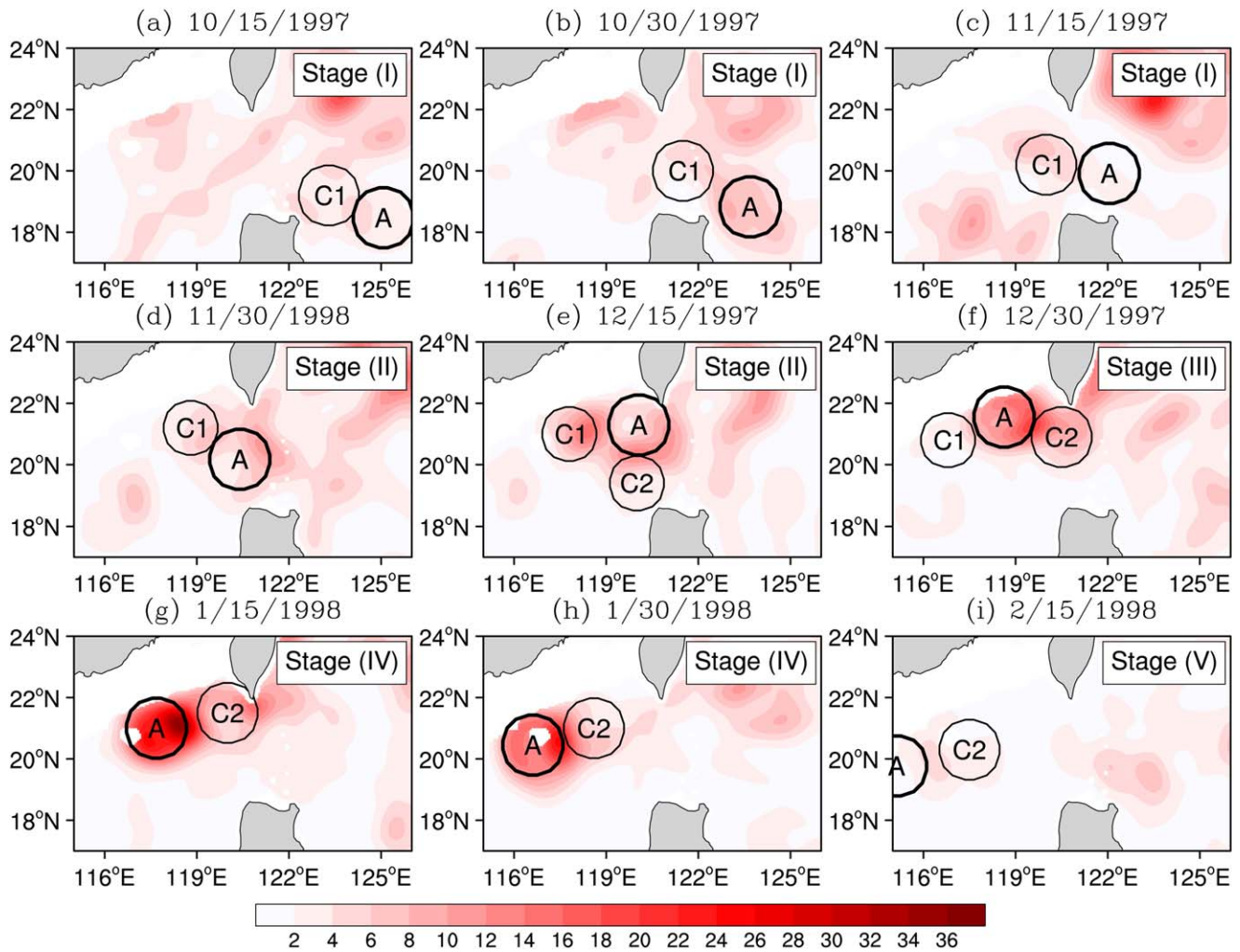


Figure 9. Same as Figure 8, but for EKE (in 10^3 J m^{-2}).

In Stage I, eddy A experiences both an increase and a decrease in energy. Correspondingly, as shown in the BC maps, to the east of Luzon, there is a BC hotspot south of 18°N and a negative center to the north (Figures 11a and 11b). Eddy A is mostly within the hotspot region just outside of the Kuroshio (Figure 11a). In

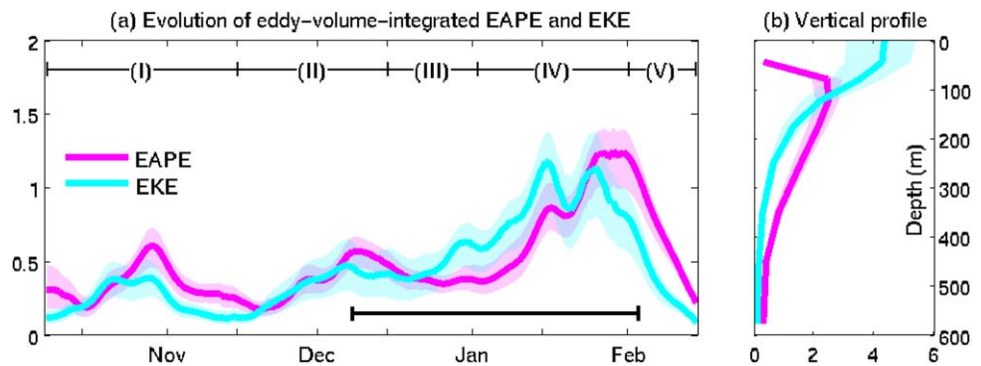


Figure 10. (left) Time series of the eddy-volume-integrated EAPE and EKE (in 10^{15} J) and (right) vertical profiles of eddy-area-integrated EAPE and EKE (in 10^{12} J m^{-1}). Other radii (100 and 150 km) have also been used for integration, and the results form the bounds of the shaded area in the figure. Five stages are marked in the left figure.

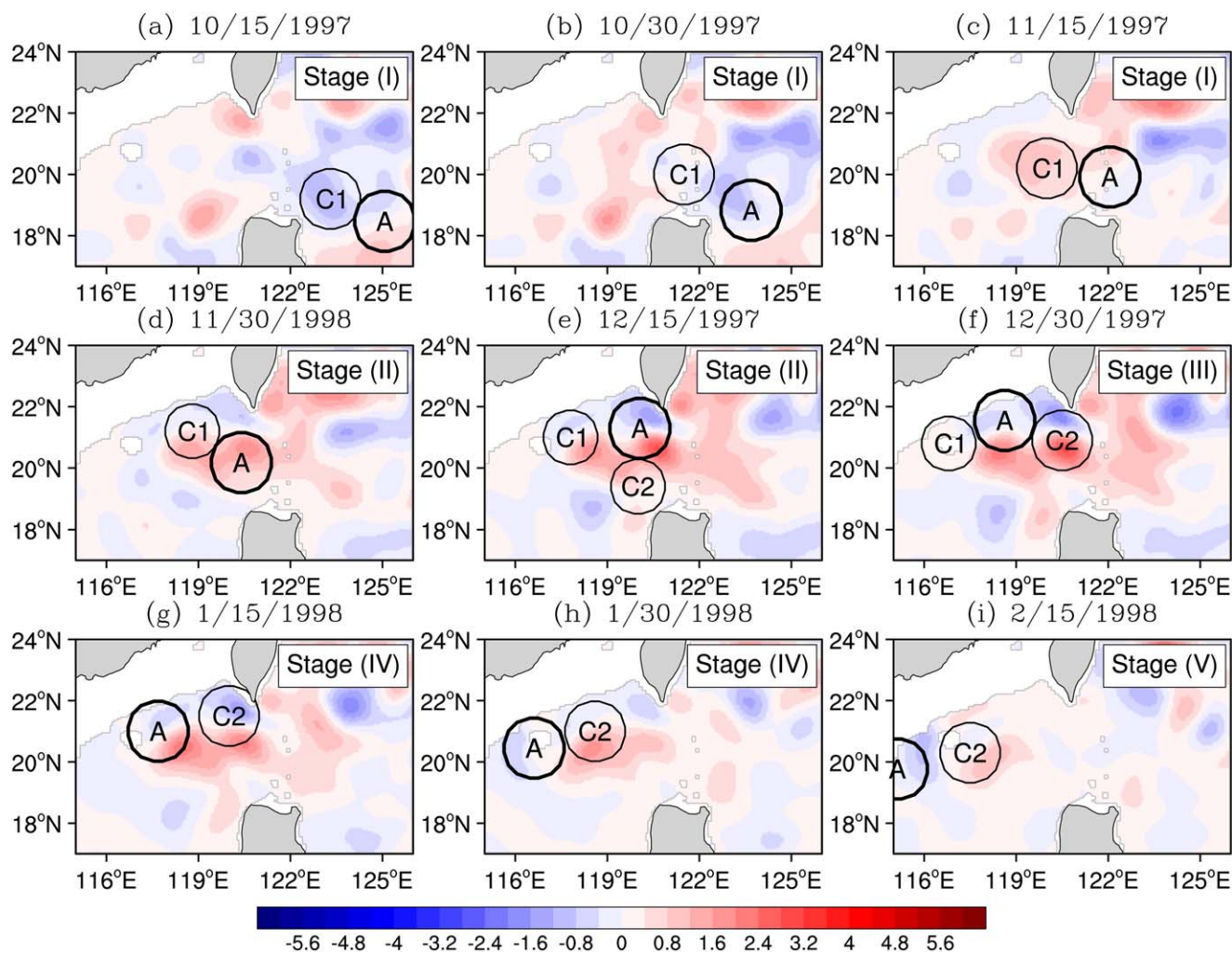


Figure 11. Vertically integrated BC (in 10^{-2} W m^{-2}). The eddies are marked in black circles.

general, eddy A undergoes a baroclinic instability, removing APE from the background field and forming the first peak in the EAPE time series (Figure 10a). As the eddy moves west and northward influenced by the western boundary current, it moves into the negative BC area (Figure 11b), which causes an upscale APE cascade and a decrease in EAPE (Figure 11c). In Stage II, eddy A crosses the Kuroshio, encountering the relatively stationary positive BC region (Figure 11d). The APE from the large-scale window thus fuels its growth, generating the second peak in the EAPE time series (Figure 10a). From the middle to the end of December, eddy A continues to grow due to the positive BC (Figure 11e). However, the transfer strength is weaker than that in the previous stage. Meanwhile, southwest of eddy A, a cold eddy C2 develops in the quasi-stationary BC region. This eddy grows rapidly and moves northward, leading to the detachment of eddy A (Figure 11f). After detaching from the Kuroshio, eddy A propagates to the southwest along the continental shelf, encountering the quasi-stationary BC region for a second time (Figure 11g), which causes another enhancement, leading to the third peak in the EAPE time series (Figure 10a). In the final stage, the eddy passes Dongsha, and in the west of the islands where BC is negative, it experiences an inverse APE cascade (Figures 11h and 11i). There, EAPE is transferred back into the mean flow, which partially leads to the demise of the eddy.

5.3.2. Barotropic Transfer (BT)

The vertically integrated BT maps are shown in Figure 12, which have a similar temporal evolution pattern to BC maps. For instance, there is also a quasi-stationary positive BT region, which is located in between the LS, emerging in mid-November 1997 and decaying in early February 1998 (Figures 12c–12i). Furthermore,

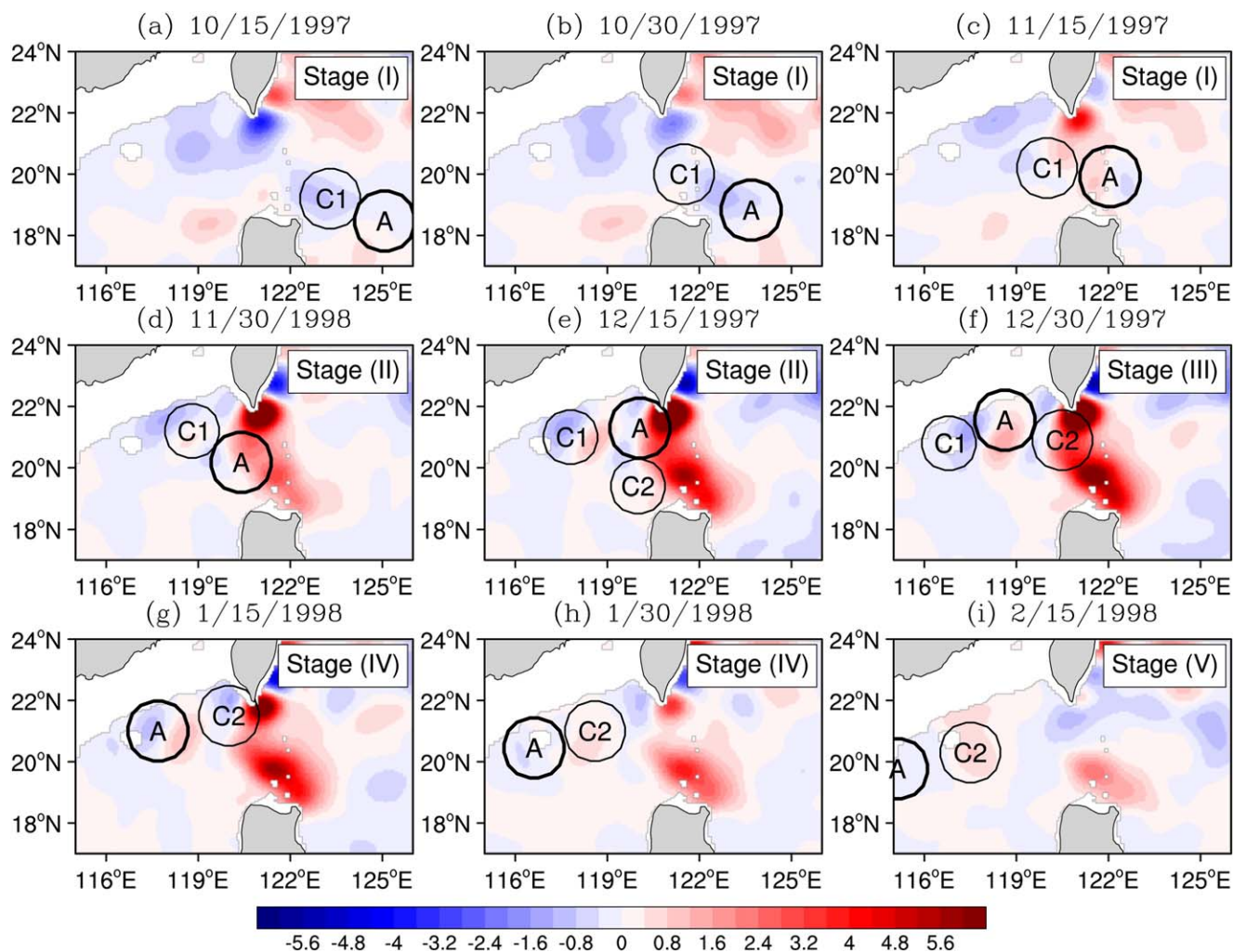


Figure 12. Same as Figure 11, but for BT (in 10^{-2} W m^{-2}).

there are several other localized centers, e.g., the negative center near Dongsha and the positive center to its east, which rarely change. The vertical profile of BT is similar to that of EKE, which is surface trapped and decays with depth (not shown).

Together, BC and BT play an important role in the evolution of eddy A. In Stage I, both eddy C1 and eddy A encroach the Kuroshio main current from the east. In the interaction region, BT is negative overall (Figures 12a and 12b), implying an upscale cascade of KE, and thus, the weakening of these two eddies. By mid-November, eddy A moves into the quasi-stationary BT region (Figure 12c) and begins to extract kinetic energy from the large-scale flow to feed itself. This interaction continues as it moves to the north (Figures 12d and 12e). Meanwhile, eddy C2 is formed north of Luzon and grows rapidly due to the BT (Figure 12e). As it develops and moves to the north, it cuts off eddy A from the Kuroshio main current (Figure 12f). By mid-January, eddy A approaches Dongsha, entering the negative BT area (Figure 12g). EKE is transferred back into the large-scale window, weakening the eddy strength and finally leading to its demise (Figures 12h and 12i).

5.3.3. Buoyancy Conversion (*b*)

Buoyancy conversion (*b*) links APE and KE on each individual scale window. Here, we only study mesoscale conversion b^1 . Compared to the relatively stationary BC and BT, mesoscale conversion is much more energetic. Moreover, it tends to move in unison with the eddies. An observation is that b^1 is generally maximized in the eddy regions and is insignificant elsewhere (Figure 13).

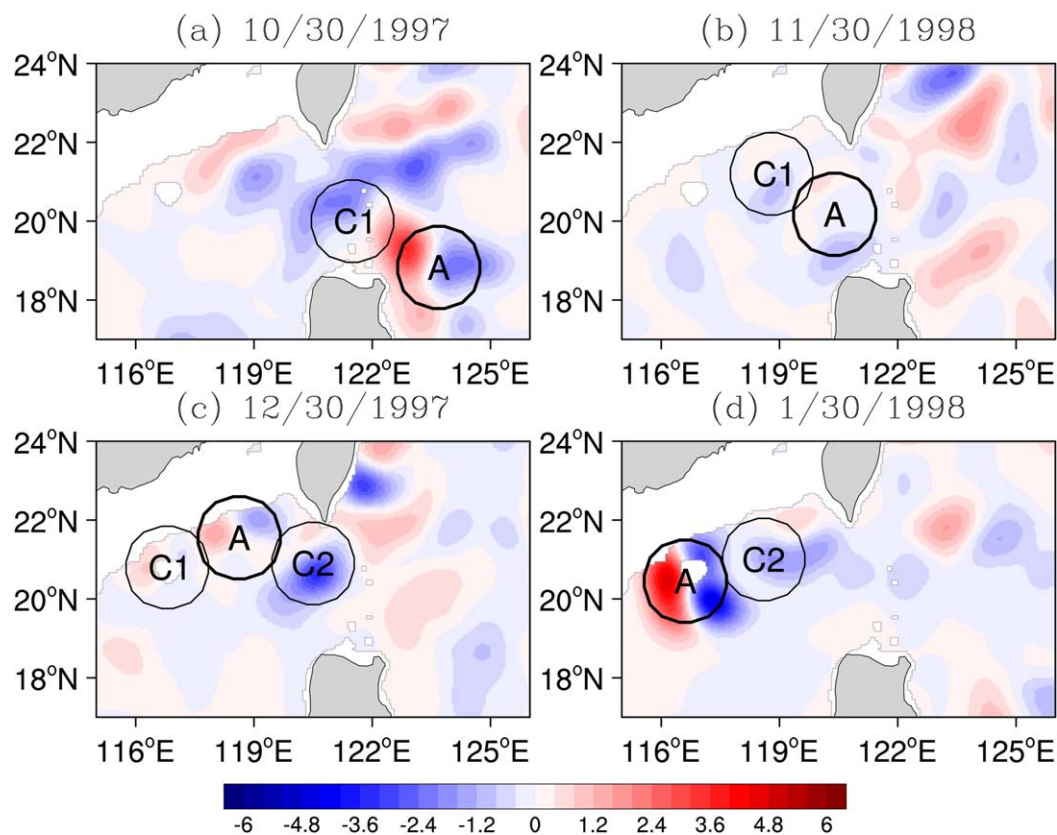


Figure 13. Same as Figure 11, but for buoyancy conversion (b , in 10^{-2} W m^{-2}).

5.3.4. Quantitative Energy Transfer and Conversion

To further delineate the energy transfer and conversion processes, we quantitatively determine the eddy-volume-integrated BC, BT, and b^1 for eddy A. The scheme follows the one used for EAPE and EKE.

The computed APE and KE transfer and conversion rates are presented in the box diagrams in Figure 14. The result shows that although b^1 has strong centers on the horizontal maps (Figure 13), the overall amount within the eddy column is weaker than BC and BT. Moreover, the conversion direction frequently changes. The directions of the two transfers are mostly the same and the transfer strengths roughly covary with each other. In Stage I (Figures 14a and 14b), during which eddy A is weakened, the transfer, as a whole, occurs from the mesoscale to the large-scale windows. In mid-October, the two transfers are weak, whereas b^1 is strong. The rate of conversion from EAPE to EKE is $1.74 \times 10^8 \text{ W}$ (Figure 14a). On 30 October, the volume-integrated BC and BT increase to values as large as $1.78 \times 10^8 \text{ W}$ and $1.28 \times 10^8 \text{ W}$, respectively (Figure 14b). In other words, the total APE and KE transferred from the mesoscale to large-scale fields reach $1.54 \times 10^{13} \text{ J}$ and $1.11 \times 10^{13} \text{ J}$ per d, which are equivalent to 3.23% and 4.14% of the total APE and KE of the eddy at that time, respectively. Early in Stage II, b^1 is maximized as eddy A penetrates the Kuroshio (Figure 14c), reaching $2.24 \times 10^8 \text{ W}$. Afterward, b^1 generally remains low. At this time, BC and BT both reverse directions, becoming favorable to eddy growth. BC attains its maximum on 30 November (Figure 14d), with a transfer rate of $4.73 \times 10^8 \text{ W}$, which is equivalent to $4.08 \times 10^{13} \text{ J}$ per d, or 11.02% of the total eddy APE at that time. Later on, BT is maximized in mid-December, reaching a value as large as $1.23 \times 10^9 \text{ W}$ (Figure 14e), which is equivalent to $1.07 \times 10^{14} \text{ J}$ per d, or 25.07% of the total eddy KE. By the time of the shedding (Figure 14f), both BC and BT have been significantly attenuated. However, in the middle of January 1998 (Figure 14g), BC attains a second local maximum, whereas BT reverses its direction. In the final stage, the upscale energy cascade dominates, especially when the eddy passes the Dongsha Islands (Figures 14h–14i). The energy transferred from the eddy to the large-scale field is estimated to be $2.21 \times 10^{13} \text{ J}$ and $9.16 \times 10^{12} \text{ J}$ per d (Figure 14i), equivalent to 5.06% and 5.17% of the total eddy APE and KE at that time, respectively. Overall, both BC and

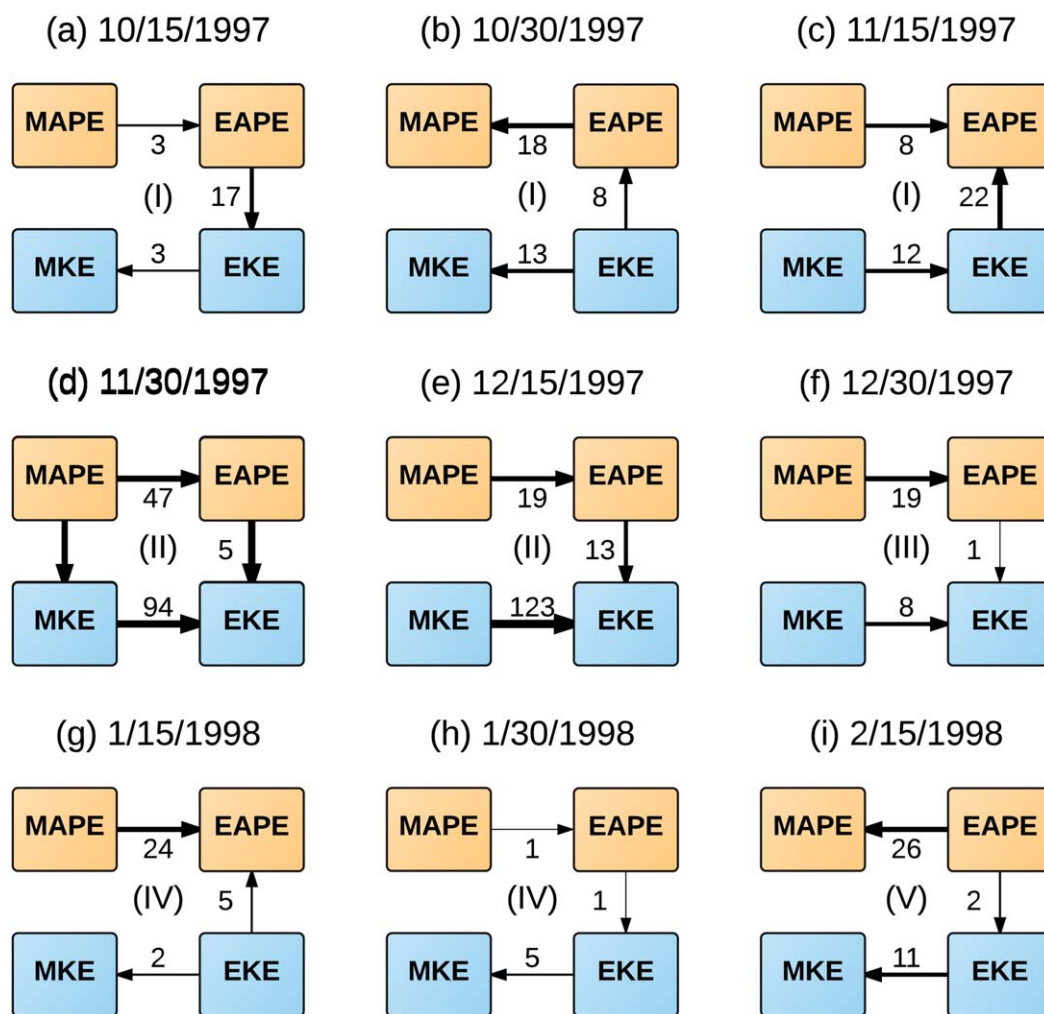


Figure 14. Box diagram of eddy-volume-integrated transfers and conversions (in 10^7 W).

BT play important roles in this eddy-shedding event. Specifically, BT greatly affects the eddy as it nears the Kuroshio main current, whereas BC dominates when the eddy is far away. This scenario is quite different from that in *Jia et al.* [2005], which states that the energy for the eddy-shedding process comes primarily from the frontal instability of the Kuroshio.

5.4. Energy Balance

In this section, we analyze the energy balance following the path of anticyclonic eddy A.

5.4.1. EAPE Balance

It is clear from the time series of the integrated energetics, as shown in Figure 15, that BC, b^1 , and the horizontal advection of APE ($\Delta_h Q_A^1$) dominate in the APE balance and the vertical APE transport ($\Delta_z Q_A^1$) is negligible. The most conspicuous term is BC, which determines the evolution of the eddy's APE. In Stage II and Stage III, the eddy is rich in EAPE; thus, the conversion from EAPE to EKE dominates. In Stage IV, b^1 is mainly from EKE to EAPE, whereas in the final stage, the direction is reversed. The horizontal advection, $\Delta_h Q_A^1$, also has five clear regimes, although they differ slightly from that of BC. Before the eddy penetrates the Kuroshio, the EAPE transport is overall negative in the eddy, which may be due to the strong downstream advection of EAPE by the mean flow. From late November to the time of eddy-shedding, $\Delta_h Q_A^1$ causes EAPE to accumulate in the eddy area. This together with BC makes the eddy grow. In Stage IV, $\Delta_h Q_A^1$ functions to compensate BC. When the eddy passes Dongsha (from late January to early February), BC and b^1 are weak, whereas $\Delta_h Q_A^1$ is rather strong. This implies that it is the APE transport by $\Delta_h Q_A^1$ from the ambient field that

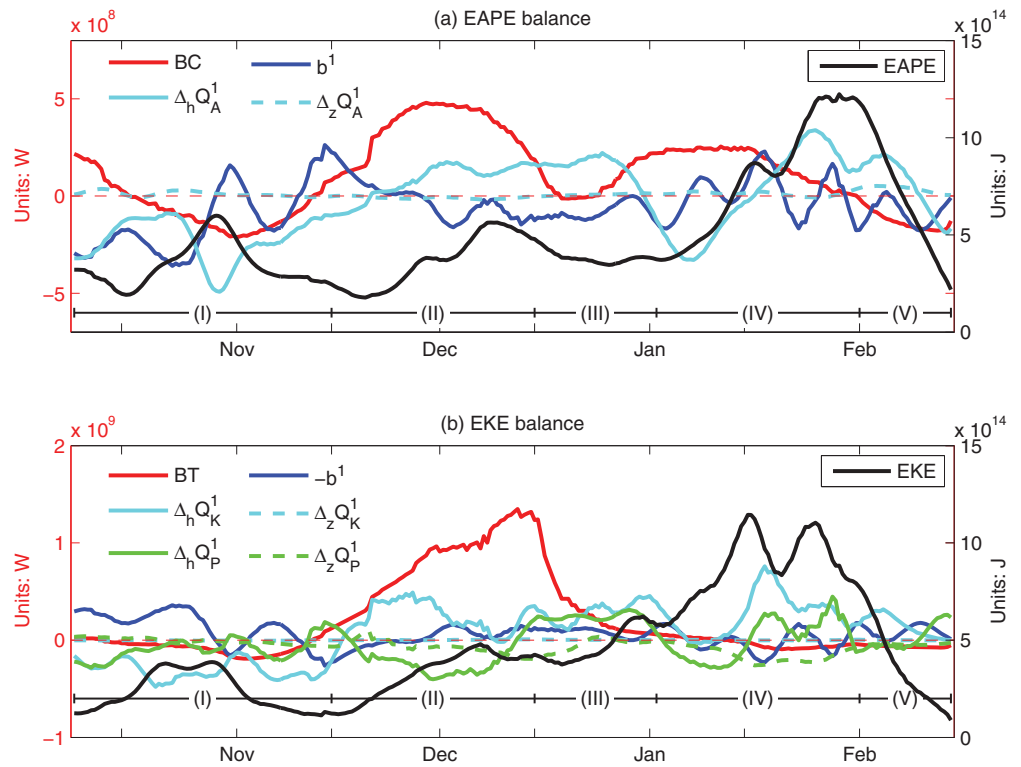


Figure 15. (top) Evolution of EAPE terms with time (in W), (bottom) Evolution of EKE terms with time (in W).

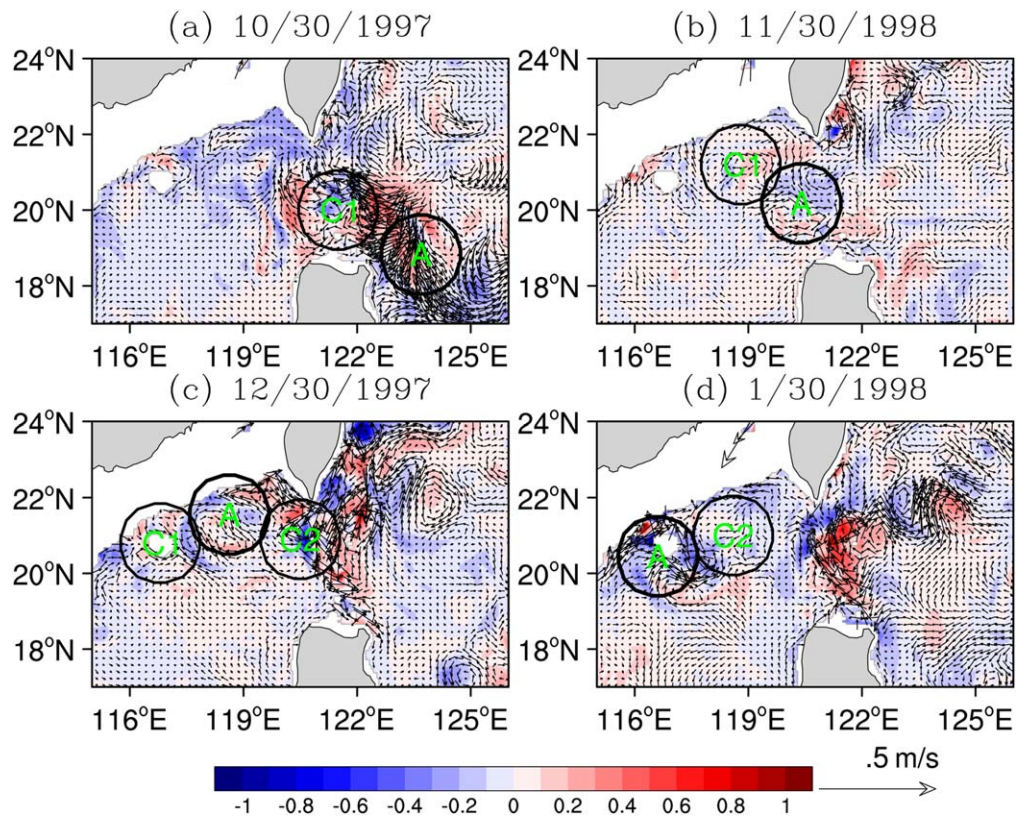


Figure 16. Same as Figure 5, but for sub-mesoscale fields.

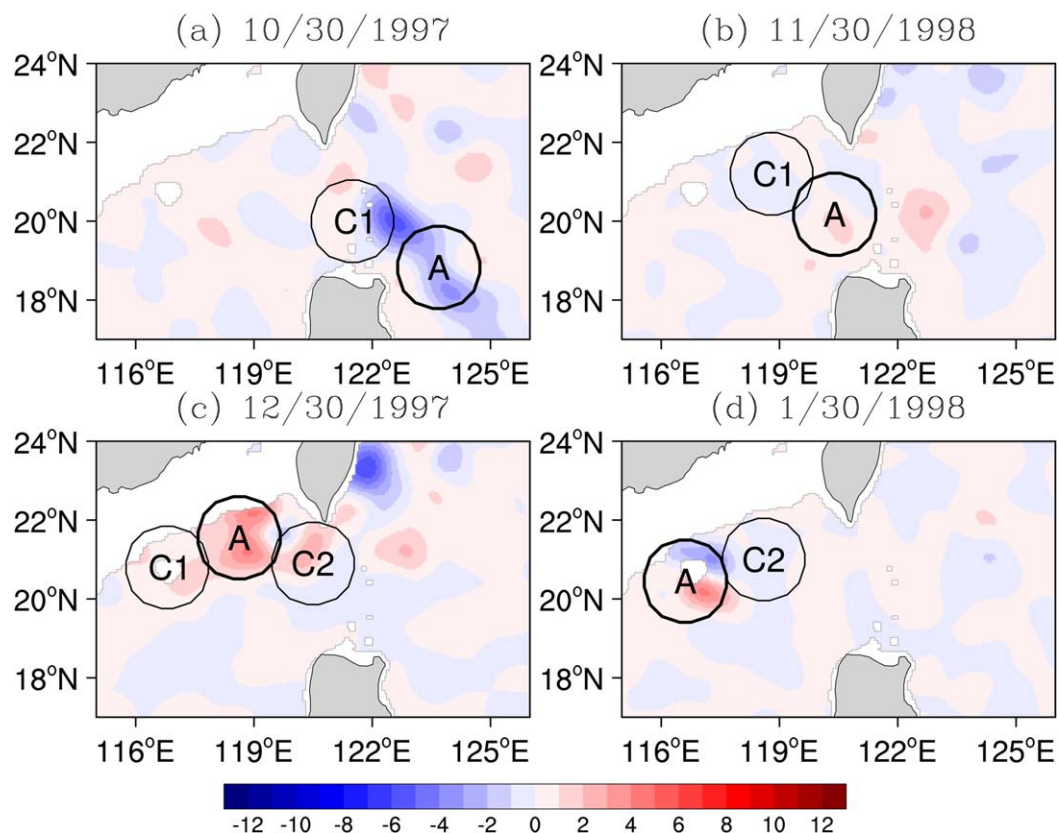


Figure 17. Vertically integrated BC from mesoscale to sub-mesoscale (in 10^{-3} W m^{-2}).

causes the rapid growth of the eddy's APE during a time when EKE diminishes (cf. Figures 8–10). After the eddy passes the islands, all mechanisms act to weaken it.

5.4.2. EKE Balance

In the KE balance, the important processes are BT, horizontal KE advection ($\Delta_h Q_K^1$), horizontal pressure working ($\Delta_h Q_p^1$), and b^1 (Figure 15b), whereas the vertical components of advection ($\Delta_z Q_K^1$) and pressure work ($\Delta_z Q_p^1$) are insignificant. The most notable feature of these time series is the overwhelmingly large BT during the eddy's development period. The evolution of $\Delta_h Q_K^1$ is, to a large extent, similar to that of $\Delta_h Q_A^1$. In Stage I, b^1 and $\Delta_h Q_K^1$ dominate and almost offset each other. BT and $\Delta_h Q_p^1$ are relatively weak, but they both act to weaken the eddy. In Stage II, the eddy is located in the most barotropically unstable area. BT, together with $\Delta_h Q_K^1$ and b^1 , contributes to the eddy's rapid growth. In Stage III, the eddy moves away from the BT hotspot. However, almost all terms in the KE equation continue to support EKE growth. In Stage IV, BT, though weak, becomes negative. The eddy grows again due to $\Delta_h Q_K^1$ and $\Delta_h Q_p^1$. Finally, all terms become small and the eddy eventually diminishes.

In summary, as eddy A evolves temporally and in size, BC and BT dominate the EAPE and EKE balances, respectively, though transports may take effect during some periods. That is to say, barotropic and baroclinic instabilities are the major mechanisms underlying the shedding of the anticyclonic eddy.

6. Potential Role of Sub-Mesoscale Processes

So far, we have not discussed the potential influence of sub-mesoscale processes, which could be important. However, in this study, the daily nudging may have interfered with these processes. Here, we briefly discuss their potential influence.

Figure 16 shows the reconstructed sub-mesoscale velocity and temperature fields at 250 m, which generally have small magnitudes. However, significant amplification is observed during certain times and locations, which may be related to the specific mesoscale eddy under investigation (e.g., Figures 16a and 16c). In the

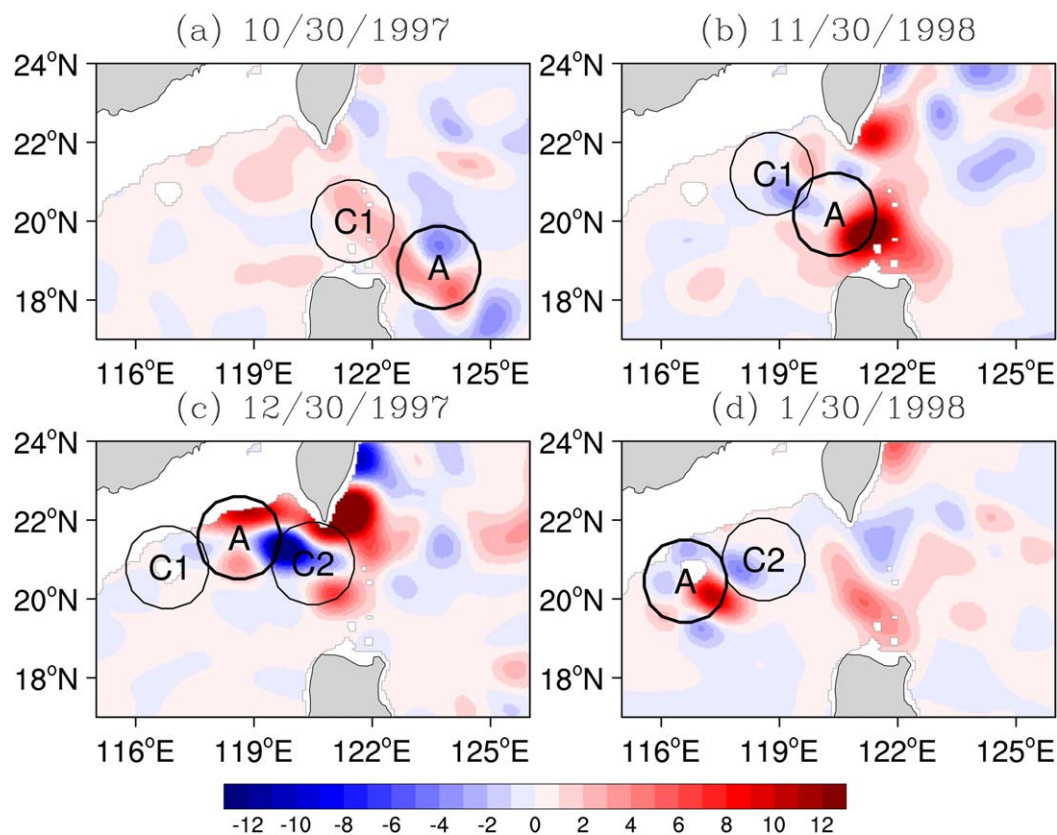


Figure 18. Same as Figure 17, but for BT (in 10^{-3} W m^{-2}).

following paragraph, we examine the effects of sub-mesoscale processes by studying the energy transfer between the mesoscale and sub-mesoscale windows.

Figures 17 and 18 show the vertically integrated BC and BT from the mesoscale window to the sub-mesoscale window, respectively. These transfer centers correspond well with the mesoscale eddy areas and intensive sub-mesoscale activities. For example, as eddy A crosses the western boundary current (WBC), the mesoscale field experiences a secondary baroclinic stability, with the available potential energy transferred back to the mesoscale field (Figure 17a). Alternatively, the mesoscale field experiences a strong secondary barotropic instability when eddy A approaches WBC, which transfers kinetic energy to the sub-mesoscale perturbation (Figure 18a). This instability intensifies the sub-mesoscale activity, which can be seen on the velocity map (Figure 16a). Later on, when eddy A approaches the Dongsha Islands, the mesoscale field experiences a secondary mixed instability and the energy cascades to the sub-mesoscale window (Figures 17c and 18c). As mentioned above, we do not have suitable data for a reliable reconstruction of the sub-mesoscale window. However, if these scenarios are true, these instabilities will be topics of much interest. Nonetheless, as the magnitudes between the two larger-scale windows are almost one order smaller than their counterparts, we currently have a good reason to neglect their contribution to the LS eddy-shedding, at least to the zeroth order.

In this study, we avoid talking about the role of dissipation since it is usually pronounced in the sub-mesoscale window which, as mentioned above, we cannot reliably reconstruct. Moreover, these terms in the governing equations are still empirically formulated and depend on the set parameters. For this reason, we have focused on the nonlinear interactions and leave these processes for future study.

7. Conclusions

Using a new methodology, the localized multiscale energetics analysis, which is a part of MS-EVA, we diagnosed the nonlinear dynamical processes underlying a typical eddy shedding as the Kuroshio loops around the Luzon Strait (LS) during late 1997 through early 1998.

Through multiscale window transform, the dynamic features are reconstructed on both a large-scale window and a mesoscale window, with the latter characterizing the eddy event. According to the mesoscale window, the shed eddy originates in the Northwest Pacific and is not generated in the loop area. Initially, a strong cold eddy travels westward from the Northwest Pacific, followed by a warm eddy. As they approach the western boundary, they interact with the Kuroshio and transfer both APE and KE upscale to the mean flow, and then weaken. Nevertheless, both of them survive. After passing through the stream, a strong mixed instability (baroclinic and barotropic) causes the eddies, especially the warm eddy, to develop rapidly, which then move northwestward. The more mature warm eddy has a calculated scale of 250 km in diameter and more than 500 m in depth, and moves at a speed of 0.15 m s^{-1} , in agreement with that of the first Rossby wave mode. Meanwhile, another cold eddy is generated, to the southeast of the warm eddy, also through a strong mixed instability. In its development, the cold eddy moves northward, cutting the warm eddy off the Kuroshio main current. Subsequently, the three eddies travel toward Dongsha and diminish to the west of the islands.

We also find that both the Kuroshio and Luzon Cold Gyre (LCG) on the large-scale window vary seasonally. From September 1997 through the end of February 1998, the Kuroshio takes, in sequence, a loop path, a leaking path, and a leaping path. The corresponding large-scale kinetic energy (MKE) and available potential energy (MAPE) first strengthen, and then, weaken. In contrast to MKE, which is surface-trapped, MAPE is concentrated at middle depths.

On the mesoscale window, all kinetic energetic terms tend to be surface-trapped in the vertical direction. In contrast, their available potential counterparts are concentrated at middle depths. Horizontally, EKE is minimized at the eddy centers and maximized at their outer rims, whereas EAPE decreases concentrically from the centers. Generally, these terms have their respective distributions moving in unison with the eddies; in contrast, BC and BT between the mean and eddy windows usually have relatively fixed spatial patterns. This result proves, similar to our previous work, that BC and BT indeed reflect the intrinsic dynamics, which are fundamental to the observed processes. Figure 14 gives a quantitative time evolution of the multiscale energetics of the shedding event.

We emphasize that this study concerns one event only. Although shedding events are typically the same, the eddy-shedding may differ on a case-by-case basis. We do not claim that the obtained dynamic processes are generic. Nonetheless, we hope that we can gain some understanding of this highly nonlinear geophysical dynamical phenomenon.

Acknowledgments

We are grateful to the two anonymous reviewers for their comments, which helped improve the manuscripts. The authors would like to thank the data and codes providers, which made this work possible. Specifically, the AVISO SSH data can be downloaded from <ftp://ftp.aviso.oceanobs.com>, the ROMS source codes are available at <http://www.romsagrif.org/>, the HYCOM reanalysis data are available at <http://hycom.org/>, and the CFSR wind stress and heat-flux fields can be downloaded from <https://climatedataguide.ucar.edu/climate-data/climate-forecast-system-reanalysis-cfsr>. The package of the MS-EVA programs is available upon request. The ROMS outputs used to plot the figures in this work can be obtained from Y. B. Zhao through email (zhaoyuanbing88@126.com). Most of the figures in this paper were created with the NCAR Command Language (NCL). This work was supported by the National Science Foundation of China (NSFC) under grant 41276032, by Jiangsu Provincial Government through the 2015 Jiangsu Program of Entrepreneurship and Innovation Group and the Jiangsu Chair Professorship, and by State Oceanic Administration through National Program on Global Change and Air-Sea Interaction (GASI-IPOVAI-06).

References

- Barrett, J. R. (1971), Available potential energy of Gulf Stream rings, *Deep Sea Res. Oceanogr. Abstr.*, 18(12), 1221–1231.
- Caruso, M. J., G. G. Gawarkiewicz, and R. C. Beardsley (2006), Interannual variability of the Kuroshio intrusion in the South China Sea, *J. Oceanogr.*, 62(4), 559–575.
- Chelton, D. B., M. G. Schlax, R. M. Samelson, and R. A. De Szoeke (2007), Global observations of large oceanic eddies, *Geophys. Res. Lett.*, 34, L15606, doi:10.1029/2007GL030812.
- Chern, C.-S., and J. Wang (1998), A numerical study of the summertime flow around the Luzon Strait, *J. Oceanogr.*, 54(1), 53–64. [Available at <http://dx.doi.org/10.1007/BF02744381>.]
- Chern, C.-S., S. Jan, and J. Wang (2010), Numerical study of mean flow patterns in the South China Sea and the Luzon Strait, *Ocean Dyn.*, 60(5), 1047–1059. [Available at <http://dx.doi.org/10.1007/s10236-010-0305-3>.]
- Chu, X., H. Xue, Y. Qi, G. Chen, Q. Mao, D. Wang, and F. Chai (2014), An exceptional anticyclonic eddy in the South China Sea in 2010, *J. Geophys. Res. Oceans*, 119, 881–897, doi:10.1002/2013JC009314.
- Cummings, J. A. (2005), Operational multivariate ocean data assimilation, *Q. J. R. Meteorol. Soc.*, 131(613), 3583–3604.
- Farris, A., and M. Wimbush (1996), Wind-induced Kuroshio intrusion into the South China Sea, *J. Oceanogr.*, 52(6), 771–784. [Available at <http://dx.doi.org/10.1007/BF02239465>.]
- Fox, D. N., W. J. Teague, C. N. Barron, M. R. Carnes, and C. M. Lee (2002), The Modular Ocean Data Assimilation System (MODAS), *J. Atmos. Oceanic Technol.*, 19(2), 240–252.
- Gan, J., Li, H., E. N. Curchitser, and D. B. Haidvogel (2006), Modeling South China Sea circulation: Response to seasonal forcing regimes, *J. Geophys. Res.*, 111, .
- Gill, A. E., J. S. A. Green, and A. J. Simmons (1974), Energy partition in the large-scale ocean circulation and the production of mid-ocean eddies, *Deep Sea Res. Oceanogr. Abstr.*, 21(7), 499–508.
- Hu, J., H. Kawamura, H. Hong, and Y. Qi (2000), A review on the currents in the South China Sea: Seasonal circulation, South China Sea warm current and Kuroshio intrusion, *J. Oceanogr.*, 56(6), 607–624.
- Jia, Y., and E. P. Chassignet (2011), Seasonal variation of eddy shedding from the Kuroshio intrusion in the Luzon Strait, *J. Oceanogr.*, 67(5), 601–611.
- Jia, Y., Q. Liu, and W. Liu (2005), Primary study of the mechanism of eddy shedding from the Kuroshio bend in Luzon Strait, *J. Oceanogr.*, 61(6), 1017–1027.
- Kara, A. B., E. J. Metzger, H. E. Hurlburt, A. J. Wallcraft, and E. P. Chassignet (2008), Multistatistics metric evaluation of ocean general circulation model sea surface temperature: Application to 0.08° Pacific hybrid coordinate ocean model simulations, *J. Geophys. Res.*, 113, C12018, doi:10.1029/2008JC004878.

- Kuehl, J. J., and V. A. Sheremet (2009), Identification of a cusp catastrophe in a gap-leaping western boundary current, *J. Mar. Res.*, *67*(1), 25–42.
- Li, L., W. D. Nowlin, and J. Su (1998), Anticyclonic rings from the Kuroshio in the South China Sea, *Deep Sea Res., Part I*, *45* (9), 1469–1482.
- Liang, X. S. (2016), Canonical transfer and multiscale energetics for primitive and quasigeostrophic atmospheres, *J. Atmospheric Sci.*, *73*(11), 4439–4468, doi:10.1175/JAS-D-16-0131.1.
- Liang, X. S., and D. G. M. Anderson (2007), Multiscale window transform, *Multiscale Model. Simul.*, *6*(2), 437–467.
- Liang, X. S., and A. R. Robinson (2004), A study of the Iceland-faeroe frontal variability using the multiscale energy and vorticity analysis, *J. Phys. Oceanogr.*, *34* (12), 2571–2591.
- Liang, X. S., and A. R. Robinson (2005), Localized multiscale energy and vorticity analysis: I. fundamentals, *Dyn. Atmos. Oceans*, *38*, 195–230.
- Liang, X. S., and A. R. Robinson (2007), Localized multiscale energy and vorticity analysis: II. finite-amplitude instability theory and validation, *Dyn. Atmos. Oceans*, *44*(2), 51–76.
- Liang, X. S., and A. R. Robinson (2009), Multiscale processes and nonlinear dynamics of the circulation and upwelling events off Monterey bay, *J. Phys. Oceanogr.*, *39*(2), 290–313.
- Lin, X., Y. Yin, P. Zhai, and J. Yang (2014), A mechanism for the latitudinal dependence of peak-spectrum sea surface height variability, *J. Geophys. Res. Oceans*, *119*, 1431–1444, doi:10.1002/2013JC009642.
- Liu, Y., C. Dong, Y. Guan, D. Chen, J. McWilliams, and F. Nencioli (2012), Eddy analysis in the subtropical zonal band of the north Pacific ocean, *Deep Sea Res., Part I*, *68*, 54–67.
- Lorenz, E. N. (1955), Available potential energy and the maintenance of the general circulation, *Tellus*, *7*(2), 157–167.
- Lu, J., and Q. Liu (2013), Gap-leaping Kuroshio and blocking westward-propagating Rossby wave and eddy in the Luzon Strait, *J. Geophys. Res. Oceans*, *118*, 1170–1181, doi:10.1002/jgrc.20116.
- Marchesio, P., J. C. McWilliams, and A. Shchepetkin (2001), Open boundary condition for long-term integration of regional oceanic models, *Ocean Modell.*, *3* (1), 1–20.
- McCreary, J. P., and Z. Yu (1992), Equatorial dynamics in a $2\frac{1}{2}$ -layer model, *Prog. Oceanogr.*, *29*(1), 61–132.
- Metzger, E. J., and H. E. Hurlburt (2001), The importance of high horizontal resolution and accurate coastline geometry in modeling South China Sea inflow, *Geophys. Res. Lett.*, *28*(6), 1059–1062.
- Nan, F., H. Xue, F. Chai, L. Shi, M. Shi, and P. Guo (2011a), Identification of different types of Kuroshio intrusion into the South China Sea, *Ocean Dyn.*, *61*(9), 1291–1304.
- Nan, F., H. Xue, P. Xiu, F. Chai, M. Shi, and P. Guo (2011b), Oceanic eddy formation and propagation southwest of Taiwan, *J. Geophys. Res.*, *116*, C12045, doi:10.1029/2011JC007386.
- Nan, F., H. Xue, and F. Yu (2014), Kuroshio intrusion into the South China Sea: A review, *Prog. Oceanogr.*, *137*, 314–333. [Available at <http://www.sciencedirect.com/science/article/pii/S0079661114000986>.]
- Qiu, B. (1999), Seasonal eddy field modulation of the north Pacific subtropical countercurrent: TOPEX/Poseidon observations and theory, *J. Phys. Oceanogr.*, *29*, 2471–2486.
- Qu, T. (2000), Upper-layer circulation in the South China Sea, *J. Phys. Oceanogr.*, *30*(6), 1450–1460.
- Reid, R. O., B. A. Elliott, and D. B. Olson (1981), Available potential energy: A clarification, *J. Phys. Oceanogr.*, *11*(1), 15–29.
- Shaw, P. T., S. Y. Chao, and L. L. Fu (1999), Sea surface height variations in the South China Sea from satellite altimetry, *Oceanol. Acta*, *22*(1), 1–17.
- Shchepetkin, A. F., and J. C. McWilliams (2005), The regional oceanic modeling system (ROMS): A split-explicit, free-surface, topography-following coordinate oceanic model, *Ocean Modell.*, *9*(4), 347–404.
- Sheremet, V. A. (2001), Hysteresis of a western boundary current leaping across a gap, *J. Phys. Oceanogr.*, *31*(2001), 1247–1259.
- Sheremet, V. A., and J. Kuehl (2007), Gap-leaping western boundary current in a circular tank model, *J. Phys. Oceanogr.*, *37*(6), 1488–1495.
- Sheu, W. J., C. R. Wu, and L. Y. Oey (2010), Blocking and westward passage of eddies in the Luzon Strait, *Deep Sea Res., Part II*, *57*, 1783–1791.
- Strang, G., and T. Nguyen (1996), *Wavelets and Filter Banks*, 2nd ed., Wellesley-Cambridge Press, Wellesley, Mass.
- Wang, Z., D. Yuan, and Y. Hou (2010), Effect of meridional wind on gap-leaping western boundary current, *Chin. J. Oceanol. Limnol.*, *28*(2), 354–358.
- Williams, R. G., C. Wilson, and C. W. Hughes (2007), Ocean and atmosphere storm tracks: The role of eddy vorticity forcing, *J. Phys. Oceanogr.*, *37*, 2267–2289.
- Wu, C. R., and T. L. Chiang (2007), Mesoscale eddies in the northern South China Sea, *Deep Sea Res., Part II*, *54*, 1575–1588.
- Xue, H., F. Chai, N. Pettigrew, D. Xu, M. Shi, and J. Xu (2004), Kuroshio intrusion and the circulation in the South China Sea, *J. Geophys. Res.*, *109*, C02017, doi:10.1029/2002JC001724.
- Yang, D., B. Yin, Z. Liu, and X. Feng (2011), Numerical study of the ocean circulation on the East China Sea shelf and a Kuroshio bottom branch northeast of Taiwan in summer, *J. Geophys. Res.*, *116*, C05015, doi:10.1029/2010JC006777.
- Yuan, D., and Z. Wang (2011), Hysteresis and dynamics of a western boundary current flowing by a gap forced by impingement of meso-scale eddies, *J. Phys. Oceanogr.*, *41*(5), 878–888.
- Yuan, D., W. Han, and D. Hu (2006), Surface Kuroshio path in the Luzon Strait area derived from satellite remote sensing data, *J. Geophys. Res.*, *111*, C11007, doi:10.1029/2005JC003412.